Full band structure LDA and k·p calculations of optical spin-injection

F. Nastos,[1] J. Rioux,[1] M. Strimas-Mackey,[1] Bernardo S. Mendoza,[2] and J. E. Sipe[1]

[1]*Department of Physics and Institute for Optical Sciences, University of Toronto, 60 St. George Street, Toronto, Ontario, Canada M5S 1A7*

[2]*Department of Photonics, Centro de Investigaciones en Optica, León, 371500 Guanajuato, Mexico*

We present a study of optical electron spin-injection (optical orientation) in the bulk semiconductors GaAs, Si, and CdSe from direct optical excitation with circularly polarized light. For GaAs and Si, we compare pseudopotential calculations with calculations of a recent full-zone **k·p** model. For GaAs, we find that there can be up to 30% spin-injection at energies well above the band gap. For Si, which has very weak spin-orbit coupling, we find that there can be up to 30% spin polarization from direct transitions. The relatively low symmetry of wurtzite CdSe leads to an orientation dependent spin-injection, which can be up to 100% polarized at the band edge. For each of these systems, full-zone calculations are made, which allow us to consider excitation well above the band gap. An adaptive Brillouin zone sampling scheme is used, which allows us to obtain rapid convergence of our spectra. A derivation of the spin-injection rate, which accounts for the coherences excited in a semiconductor with spin-split bands, is also included.

PACS number(s): 72.25.Fe

I. INTRODUCTION

Spin-polarized electrons are injected in the conduction bands of semiconductors by the absorption of circularly polarized light. Known as *optical orientation*, this effect is a powerful tool in the field of spintronics, where it is used to generate a spin-polarized electron density in semiconductors.[1,2] At low enough energies, **k·p** methods can be used to model the process. An eight-band model successfully describes the spin-injection rate in GaAs at energies up to about 100 meV above the band edge. To describe excitation at higher energies, a 14-band **k·p** method can be used,[3] which allows the split-off bands and higher-energy conduction bands to be included. While the bands from this model are accurate up to roughly 0.5 eV away from the band edges, they drastically fail for higher energies.

Other issues limit the effectiveness of the **k·p** method. The more realistic 14-band models depend on 11 parameters, and even for GaAs, one of the most studied semiconductors, these have not been derived from a single source in a consistent manner. Some parameters come from experiment and others from theory. For the more complicated semiconductors, realistic **k·p** models are not even available.

In this work, we address the calculation of optical spin-injection from density functional theory band structures. Such *ab initio* band structures have recently been used to study other spintronic effects.[4–6] We restrict ourselves to pseudopotential band structures based on the local density approximation (LDA)+scissors correction, since this is the simplest and still the most popular approach to the calculations of optical properties using full-zone band structures. The LDA systematically underestimates the band gap, and so a band gap correction, called the "scissors correction," is implemented. This rigidly shifts the conduction band energies by a constant amount. Where possible, we contrast the LDA results with results from 30-band **k·p** models to address the validity of the **k·p** results at higher photon energies.

One technical aspect important in this work, and in many other band structure calculations, is that a large number of *k* points are required to evaluate the Brillouin zone (BZ) integrals accurately. Even using the full crystal symmetry to reduce the integration to the irreducible zone, many thousands of *k* points are needed to obtain convergence. For example, to evaluate the spin Hall spectra in GaAs, Guo *et al.*[4] used 98 790 *k* points, obtained by segmenting the ΓX line into 56 intervals. Although we find that a fine division of the BZ is also required to calculate the spin-injection tensors, the number of *k* points needed can be significantly reduced if one does not restrict oneself to an equispaced mesh of *k* points. Yao and Fang[5] took a step in this direction by implementing an adaptive scheme in which 26 *k* points are added around targeted *k* points to produce a finer mesh. Even so, they required over 2×10^6 *k* points, using a Monkhorst-Pack special points method, to obtain converged spectra. As part of this work, we present an adaptive linear analytic tetrahedral integration method. It is a straightforward extension of the widely used method of Blöchl-Jepsen-Andersen[7] (BJA) and can be used for any type of calculation involving density of states, or joint density of states. Our adaptive procedure iteratively calculates the spectrum of interest at each step refining the grid only in the area of the BZ, contributing to the frequencies of interest where the spectrum is not converged. The scheme can be easily applied to calculate other quantities relying on BZ integrals.

Another issue in calculations of this sort, when performed for noncentrosymmetric semiconductors such as GaAs, is that the energy bands are spin split in certain directions. The splitting is typically smaller than the energy width of the laser pulse, and so the pulse can excite multiple bands. This causes coherences to be excited, which must be accounted for to describe the optical spin-injection rate in these semiconductors. Bhat *et al.* had given a heuristic argument for the inclusion of coherence between spin-split bands in optical spin-injection calculations based on Fermi's golden rule.[3,6] In Sec. II of this paper, we use a density matrix approach to show, from a microscopic derivation, how the coherences are

to be included. In Sec. III, we describe the computational details involved in obtaining the relevant matrix elements and the Brillouin zone integrations. In Sec. IV, we compare the LDA results for GaAs with a recently detailed 30-band $\mathbf{k} \cdot \mathbf{p}$ model.[8,9] Our results indicate that the degree of spin polarization can be reliably calculated with LDA *ab initio* band structures. We then turn to optical orientation in other materials. We first look at absorption in bulk Si, where, to date, optical orientation has only been observed indirectly.[10] We neglect the phonon interaction, and so our results are limited to absorption across the direct band gap. We complete our study by considering optical orientation in bulk wurtzite CdSe, where the electronic structure is more complicated than in the zinc-blende crystals, and no simple full-zone $\mathbf{k} \cdot \mathbf{p}$ models exist. We summarize our results in Sec. V.

II. THEORY

In this section, we derive expressions for the spin-injection rate $\dot{\mathbf{S}}(t)$. The external laser perturbation is taken to be

$$H_{\text{ext}}(t) = -er^a E^a(t), \tag{1}$$

where e is the electron charge, $\mathbf{r}$ is the position operator, and $\mathbf{E}(t)$ is the electric field of the applied laser. The superscript Roman characters indicate Cartesian coordinates. When repeated, as in Eq. (1), the coordinates are to be summed over. We follow Adams[11] and Blount[12] to separate the interband and intraband matrix elements of the position operator. For this work, the intraband components do not play a role.

We initially consider the response to a continuous wave field,

$$\mathbf{E}(t) = \mathbf{E}(\omega)e^{-i\omega t} + \mathbf{E}^*(\omega)e^{i\omega t}, \tag{2}$$

at the level of Fermi's golden rule (FGR). Neglecting many-particle effects and phonon scattering, the spin-injection rate into the conduction bands of a clean, cold semiconductor is proportional to the field intensity,[1,13]

$$\dot{S}^a = \zeta^{abc}(\omega)E^b(-\omega)E^c(\omega). \tag{3}$$

The quantities $\zeta^{abc}(\omega)$ constitute a third rank pseudotensor. In the context of nonlinear optics, $\boldsymbol{\zeta}(\omega)$ is analogous to a second-order susceptibility, except that it is a pseudotensor instead of a tensor.

A FGR derivation gives an expression for $\zeta^{abc}(\omega)$ in terms of the band energies and matrix elements,

$$\zeta^{abc}(\omega) = \frac{2\pi e^2}{\hbar^2} \int \frac{d^3k}{8\pi^3} \sum_{c,v} S_{cc}^a(\mathbf{k}) r_{vc}^b(\mathbf{k}) r_{cv}^c(\mathbf{k}) \delta[\omega_{cv}(\mathbf{k}) - \omega]. \tag{4}$$

Italics subscripts indicate band indices. Throughout this work, c will refer to a conduction band and v to a valence band; we assume that in the ground state, the valence bands are fully occupied and the conduction states are empty. For a band m, the Bloch states $|m\mathbf{k}\rangle$ have energy eigenvalue $\hbar\omega_m(\mathbf{k})$. The quantity $\omega_{cv}(\mathbf{k})$ is defined as the difference $\omega_{cv}(\mathbf{k}) \equiv \omega_c(\mathbf{k}) - \omega_v(\mathbf{k})$. The quantity $S_{cc}^a(\mathbf{k})$ comes from the spin matrix element

$$\langle c\mathbf{k}|\hat{S}^a|m\mathbf{k}'\rangle = S_{cm}^a(\mathbf{k})\delta(\mathbf{k} - \mathbf{k}'), \tag{5}$$

and the off-diagonal dipole matrix elements $r_{cv}^a(\mathbf{k})$ are related to the velocities of the Bloch states through

$$r_{cv}^a(\mathbf{k}) = \frac{v_{cv}^a(\mathbf{k})}{i\omega_{cv}(\mathbf{k})}, \tag{6}$$

where

$$\langle c\mathbf{k}|\hat{v}^a|v\mathbf{k}'\rangle = v_{cv}^a(\mathbf{k})\delta(\mathbf{k} - \mathbf{k}'). \tag{7}$$

From Eq. (4), it can be shown that the pseudotensor $\zeta^{abc}(\omega)$ is imaginary and that it changes sign under exchange of the last two indices.[13] Here and throughout this paper, we assume, as is commonly done,[1] that the hole spins relax very quickly and we neglect them, focusing only on the electron spins; measurements have led to estimates of 110 fs for the heavy-hole spin lifetime in GaAs.[14]

One disadvantage of a FGR derivation is that it fails to capture the excited coherences. The conduction bands in the noncentrosymmetric semiconductors are spin split by a small amount,[15,16] typically smaller than the energy width of the laser pulse, and so the pulse excites a coherent superposition of the two conduction bands. Even for very long pulses with narrow energy widths, dephasing effects lead to an energy width of the bands large enough that spin-split states can become quasidegenerate. These coherences can be added in "by hand," but to more rigorously include them, we use a multiple scale approach to solve the equation of motion for the single particle density matrix $\rho_{mn}(\mathbf{k};t)$. The dynamical equation for the density matrix is

$$\frac{d\rho_{mn}(\mathbf{k};t)}{dt} = -i\hat{\omega}_{mn}(\mathbf{k})\rho_{mn}(\mathbf{k};t) - \frac{i}{\hbar}([H^{\text{ext}}(t), \rho(\mathbf{k};t)])_{mn}. \tag{8}$$

In this equation,

$$([H^{\text{ext}}(t), \rho(\mathbf{k};t)])_{mn} = H_{mp}^{\text{ext}}(t)\rho_{pn}(\mathbf{k};t) - \rho_{mp}(\mathbf{k};t)H_{pn}^{\text{ext}}(t), \tag{9}$$

where repeated level indices are summed over, and we have included the possibility of loss and dephasing in $\hat{\omega}_{mn}(\mathbf{k})$ by putting

$$\hat{\omega}_{mn}(\mathbf{k}) = \omega_{mn}(\mathbf{k}) - i\Gamma_{mn}, \tag{10}$$

where Γ_{mn} is taken to be positive.

Assuming that the conduction bands c and c' are close to one another, and that the pulse is short enough so that the energy width overlaps the two bands, the equation of motion can be solved. Leaving the details of the derivation to Appendix A, the result for the off-diagonal component $\rho_{cc'}$, where c and c' are quasidegenerate conduction states, is

$$\frac{\partial \rho_{cc'}}{\partial t} = -i(\omega_{cc'} - i\Gamma_{cc'})\rho_{cc'} + \frac{e^2 E^a(\omega)E^{b*}(\omega)}{i\hbar^2}$$

$$\times \sum_v \left(\frac{r^a_{cv} r^b_{vc'}}{\omega - \omega_{c'v} - i\epsilon} - \frac{r^a_{cv} r^b_{vc'}}{\omega - \omega_{cv} + i\epsilon} \right). \quad (11)$$

In this expression, ϵ is a small positive number, and the sum over v is limited to valence bands. The spin-injection rate can now be found from

$$\mathbf{S} = \mathrm{Tr}(\rho \hat{\mathbf{S}}). \quad (12)$$

Using the identity $(\omega - \omega_{cv} - i\epsilon)^{-1} = \mathcal{P}(\omega - \omega_{cv}) + i\pi\delta(\omega - \omega_{cv})$, where $\mathcal{P}$ indicates that the principal part should be used, we find that $\dot{\mathbf{S}}$ is still related to fields through Eq. (3), but with $\zeta^{abc}(\omega)$ now given by

$$\zeta^{abc}(\omega) = \frac{\pi e^2}{\hbar^2} \sum_{c,c',v}{}' \int \frac{d^3k}{8\pi^3} S^a_{c'c}(\mathbf{k}) r^b_{vc'}(\mathbf{k}) r^c_{cv}(\mathbf{k})$$

$$\times (\delta[\omega_{cv}(\mathbf{k}) - \omega] + \delta[\omega_{c'v}(\mathbf{k}) - \omega]) \quad (13)$$

[cf. Eq. (4)]. The prime on the summation indicates that the sum is to be done over pairs of conduction bands c and c' that are quasidegenerate. We classify bands separated by no more than 30 meV to be quasidegenerate, where the defining energy is chosen since it is approximately both a typical laser pulse energy width and the room temperature energy. In the case of degenerate bands, Eq. (13) reduces to the FGR result [Eq. (4)].

Although $\zeta^{abc}(\omega)$ is useful for understanding the total spin injected, a more physically transparent quantity useful for characterizing the spin-injection is the degree of spin polarization DSP^a defined as the average electron spin along the light propagation vector, or

$$\mathrm{DSP}^a = \frac{\dot{S}^a}{(\hbar/2)\dot{n}}, \quad (14)$$

where $\dot{n}$ is the carrier injection rate. For $\dot{n}$, the multiple scale analysis gives the same result as FGR, which can be written as

$$\dot{n} = \xi^{ab}(\omega)E^a(-\omega)E^b(\omega), \quad (15)$$

where the tensor $\xi^{ab}(\omega)$ is given by

$$\xi^{ab}(\omega) = \frac{2\pi e^2}{\hbar^2} \int \sum_{c,v} \frac{d^3k}{8\pi^3} r^a_{vc}(\mathbf{k}) r^b_{cv}(\mathbf{k}) \delta[\omega_{cv}(\mathbf{k}) - \omega]. \quad (16)$$

It is related to the imaginary part of the linear optical response tensor.[17]

III. COMPUTATIONAL DETAILS

We use both a density functional theory LDA pseudopotential band structure and a $\mathbf{k \cdot p}$ band structure to obtain the matrix elements required to calculate the spin-injection rates. It is useful to compare our LDA results to those from a different method, and we chose the $\mathbf{k \cdot p}$ method since it is one of the more popular schemes, and because it is designed to accurately replicate the experimental band structure, around Γ, with a proper choice of parameters.

A. Matrix elements: local density approximation band structures

The pseudopotential calculations are performed with the freely available ABINIT code.[18] We use the separable Hartwigsen-Goedecker-Hutter (HGH) pseudopotentials[19] within the LDA as parametrized by Goedecker et al.[20] These pseudopotentials are a common choice in *ab initio* studies investigating materials where the spin-orbit contribution cannot be neglected; see articles citing Hartwigsen et al.[19] for a collection of such studies. In our calculations, we exclude the semi-core states, as is often done, though they can be included with more computational effort. We use a cutoff of 40 hartree throughout. Once the Kohn-Sham potential is determined, we find the wave functions for k points on a specially determined tetrahedral grid. The momentum matrix elements are calculated as described by Mendoza et al.;[21] the spin matrix elements are calculated in a similar manner. The contributions to the velocity matrix elements from the nonlocal part of the pseudopotential and from the spin-orbit interaction are excluded, as is usually done. They are not readily available, and to our knowledge, no efficient scheme to include them both simultaneously has been presented. Although we know that the contributions are small for GaAs and Si, the contributions in CdSe may be substantial.[21–23]

It is well known that the density functional theory generally underestimates the band gap of insulators.[24,25] A usual approach to overcome the LDA underestimation is to use the so-called scissors correction, in which the conduction bands are all rigidly shifted up in energy by an amount that corrects the band gap. This is admittedly *ad hoc*, but the correction can be treated consistently by including a self-energy term in the Hamiltonian that adds an energy to the LDA conduction states but leaves the valence bands unchanged.[26,27] The result from an analysis of the scissors-modified Hamiltonian is that the matrix elements $r^a_{mn}(\mathbf{k})$ and $S^a_{mn}(\mathbf{k})$ are the same for both the LDA and the scissors Hamiltonian.[28,29] Since the $\hbar\omega_c(\mathbf{k})$ are shifted, the only significant consequence is in the δ function of Eq. (13) and Eq. (16), and so the spectra corresponding to the scissored Hamiltonian are obtained by simply translating in energy the spectra calculated from the LDA Hamiltonian.

B. Matrix elements: $\mathbf{k \cdot p}$ band structures

For the zinc-blende III-V materials, 14-band $\mathbf{k \cdot p}$ models are the most sophisticated models that have been used for spin-injection calculations.[3] We go beyond the 14-band model and present results using a recent 30-band model given by Richard et al.,[8] which is based on an earlier model by Cardona and Pollak.[30]

Unlike the 14-band version, which is limited in its validity to just around the Γ point, the 30-band model gives energies generally accurate over the entire Brillouin zone, in a window of 11 eV about the top of the valence band.

Richard *et al.*[8] varied 18 parameters in a fitting procedure to satisfy average zero slope of the bands at zone edge, the equivalence of the U and K points (which, unlike in the pseudopotential method, is not automatically satisfied), and overall agreement to empirical effective mass data. Only 11 nonzero parameters were necessary for GaAs, and 10 for Si, to give a satisfactory band structure. Among those parameters are the velocity matrix elements at the Γ point. The spin matrix elements at Γ are known from the basis states. We can expand the states at any $\mathbf{k}$ in terms of the zone center states, and thus the 30-band $\mathbf{k} \cdot \mathbf{p}$ model provides us with the required matrix elements over the entire Brillouin zone.

C. Brillouin zone integration

The tensor components we wish to calculate, $\zeta^{abc}(\omega)$ and $\xi^{ab}(\omega)$ [Eq. (13) and (16)], are of the form

$$G(\omega) = \sum_{c,v} G_{cv}(\omega), \tag{17}$$

with

$$G_{cv}(\omega) = \int \frac{d^3k}{8\pi^3} g_{cv}(\mathbf{k}) \delta[\omega - \omega_{cv}(\mathbf{k})]. \tag{18}$$

The δ function effectively reduces the three-dimensional integral over the Brillouin zone volume to a surface integral over the surface defined by $\omega_{cv}(\mathbf{k}) = \omega$ inside the BZ. These types of integrals are commonly referred to as "joint density of states (JDOS)-type integrals." Our goal is to accurately calculate these expressions in a frequency range relevant to optical frequencies, with $\hbar\omega$ typically between 0.5 and 4.0 eV. Higher energies are also of interest, but they are not the focus of our study. For the crystals we study here, and at the energies of interest, the constant energy surface that needs to be integrated over can be too complicated for straightforward sampling. A more efficient algorithm that is commonly used to evaluate JDOS (and density of states) integrals is the linearized analytic tetrahedron method (LATM).

To implement the LATM, the BZ needs to be divided into tetrahedra. The integrand factor $g_{cv}(\mathbf{k})$ and energy eigenvalues $\hbar\omega_m(\mathbf{k})$ are then evaluated at every tetrahedron vertex and stored. Inside each tetrahedron, the energies are linearly approximated. For a given frequency ω, the constant energy surface defined by the δ function is then identified inside each tetrahedron, and the surface integral is calculated analytically by also linearly interpolating the integrand over the tetrahedron. Summing the contributions from each tetrahedron gives the value of $G_{cv}(\omega)$.

There are various ways to generate a tetrahedral grid, but the most efficient and widely implemented scheme is the one introduced by Blöchl *et al.*[7] We implement their scheme here, but to converge the spectrum with respect to number of k points, we use a refinement technique employing an adaptive mesh. Adaptive Brillouin zone integration schemes have been presented before. For example, Wang *et al.*[31] presented a recursive tree method for three-dimensional BZ integration. Although their method includes features from finite el-

ement methods, it requires defining the irreducible wedge by hand. Later, Henk[32] demonstrated how adaptive mesh refinement could be used to speed up two-dimensional BZ integrations. Since the details required to produce our grid are not needed to follow the remainder of the main text, we present them in Appendix B.

IV. RESULTS

A. GaAs

The first material we consider is GaAs. The band structure is well understood, and the spin-injection at the band edge is known to be 50% spin polarized. As well, the 30-band $\mathbf{k} \cdot \mathbf{p}$ method band structure agrees relatively well with the pseudopotential band structure, so calculating the spin-injection allows for a direct comparison of the two methods. The unit cell is chosen so that the Ga atom is at $(0,0,0)$ and that the As atom is at $(a/4, a/4, a/4)$, where a is the conventional unit cell parameter. We have made two LDA calculations, one using the experimental (room temperature) lattice constant $(a = 10.68a_0)$ and the other using the theoretical (ground state LDA energy minimizing) lattice constant $(a = 10.45a_0)$. For the second calculation, we find a LDA band gap of 1.01 eV. Our lattice constant and band gap agree with those found by Wang and Ye,[33] who also used the HGH pseudopotentials. We use a scissor shift of 0.509 eV to adjust the LDA band gap, so that we have agreement with the $\mathbf{k} \cdot \mathbf{p}$ method band gap. For the first calculation, we also shift the band gap to 1.519 eV to aid in the comparison of the spectra, despite the fact that the band gap of a room temperature crystal is actually 1.42 eV. Using a different scissor shift, in order to obtain a band gap of 1.42 eV, would keep the shape of the spectrum the same and only rigidly shift it in energy.

We consider the absorption of left-circularly polarized light propagating along the $-\hat{z}$ direction, for which the electric field polarization is

$$\mathbf{E}(\omega) = E_0(\hat{x} - i\hat{y})/\sqrt{2}. \tag{19}$$

With this polarization, the carrier injection rate is

$$\dot{n} = \xi^{xx}(\omega)|E_0|^2, \tag{20}$$

where we have used that for the face-centered-cubic (fcc) crystals, the only nonzero components of $\xi^{ab}(\omega)$ are

$$\xi^{xx}(\omega) = \xi^{yy}(\omega) = \xi^{zz}(\omega). \tag{21}$$

To calculate the spin-injection rate, we use that the only nonzero components of $\zeta^{abc}(\omega)$ for fcc crystals are

$$\zeta^{xyz}(\omega) = \zeta^{yzx}(\omega) = \zeta^{zxy}(\omega) = -\zeta^{xzy}(\omega) = -\zeta^{yxz}(\omega) = -\zeta^{zyx}(\omega). \tag{22}$$

With the same polarization, Eq. (19), the spin-injection rate is given by

$$\dot{S}^z = \text{Im}[\zeta^{xyz}(\omega)]|E_0|^2. \tag{23}$$

In Fig. 1, we present the $\xi^{xx}(\omega)$ spectrum for GaAs using the $\mathbf{k} \cdot \mathbf{p}$ method and the two calculations based on pseudopotential band structures.[17] We plot these two LDA spectra to

FULL BAND STRUCTURE LDA AND $\mathbf{k} \cdot \mathbf{p}$...
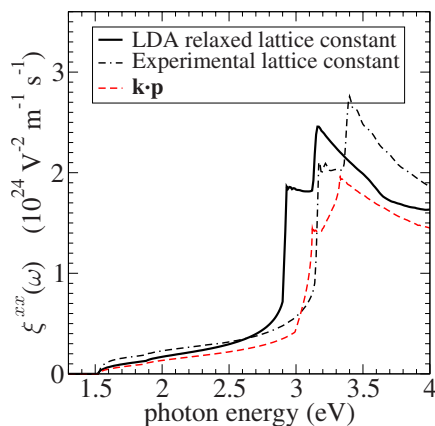
PHYSICAL REVIEW B **76**, 205113 (2007)

FIG. 1. (Color online) A comparison of $\xi^{xx}(\omega)$ calculated with the $\mathbf{k} \cdot \mathbf{p}$ and LDA band structures (Ref. 17). One LDA calculation sets the lattice constant to the experimental value (dash-dotted black line), and the other uses the LDA relaxed lattice constant (solid black line). The LDA based calculations generally overestimate the $\mathbf{k} \cdot \mathbf{p}$ calculations (dashed red line).

FIG. 2. (Color online) Comparison of $\zeta^{xyz}(\omega)$ calculated with the $\mathbf{k} \cdot \mathbf{p}$ (dashed red line) and LDA (solid black line) band structures. At most photon energies, the LDA spectrum is larger. The different peak positions between 2.9 and 3.4 eV are due to the different energy gap separations in the Γ-L region found by the two methods.

demonstrate that there is a significant difference in the spectra calculated with the two different lattice constants. Since the parameters of the $\mathbf{k} \cdot \mathbf{p}$ method are chosen to fit the empirical spectra below 2.0 eV, for purposes of comparison, we consider this spectrum to be the closest to the experimental data. However, we note that while the $\mathbf{k} \cdot \mathbf{p}$ parameters given by Richard *et al.*[8] give the correct effective mass, the value of the interband coupling matrix parameter E_P=22.37 eV is different than in other $\mathbf{k} \cdot \mathbf{p}$ models.[34,35]

Even though the spectrum calculated with the LDA relaxed lattice constant is closer to the $\mathbf{k} \cdot \mathbf{p}$ results at these experimentally relevant energies, it is too high by about 20%. This difference can be accounted for by considering the difference in effective masses. Related to the LDA underestimation of the band gap is the fact that the LDA effective masses are smaller than the $\mathbf{k} \cdot \mathbf{p}$ ones. Assuming that the heavy-hole, light-hole, and lowest conduction bands are the dominant contributions in the effective mass sum rule, at these energies, the smaller effective mass from the LDA leads to larger oscillator strengths than are realistic. In a simple model, the spectrum is directly proportional to the oscillator strength, and so it is not surprising that the LDA spectrum is too large. The spectrum calculated using the experimental lattice constant is further from the $\mathbf{k} \cdot \mathbf{p}$ one than that using the LDA. The experimental lattice constant is larger than the LDA one, and using it is analogous to considering a system with expansive strain.

It is common to see optical response studies based on *ab initio* band structures using either the experimental[36,37] or theoretical[38,39] lattice constant. The choice usually depends on the exact property being calculated and the intentions of the study. Pulci *et al.*[40] have already noted that the calculated band gap is very sensitive to the choice of lattice constant. Our calculations show that the choice can have serious consequences for the calculation of the properties near the band edge as well. In the rest of this paper, we use the LDA relaxed lattice constant for GaAs calculations, only because
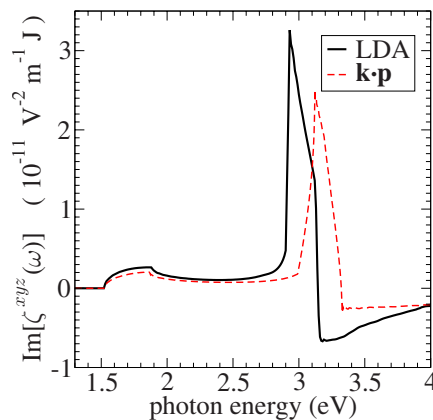
it provides more realistic behavior near the band edge.

In Fig. 2, we show the spin-injection tensor component $\zeta^{xyz}(\omega)$ calculated using the pseudopotential and $\mathbf{k} \cdot \mathbf{p}$ methods. We see that at low energies, the LDA $\zeta^{xyz}(\omega)$ spectrum is roughly 20% larger than the $\mathbf{k} \cdot \mathbf{p}$ one. The origin of this discrepancy between the LDA result and the $\mathbf{k} \cdot \mathbf{p}$ result is the same as in the $\xi^{xx}(\omega)$ difference discussed above; it is mainly due to the larger oscillator strength of the LDA. At approximately 350 meV above the band edge, there is a dip in the spectrum, which we discuss below. At higher energies, around 3.1 eV, we see that $\zeta^{xyz}(\omega)$ is quite large. This is due to transitions in the Γ-L valley region of the BZ, where there is a large joint density of states. However, from the value of $\zeta^{xyz}(\omega)$ alone, it is unclear whether one is injecting electrons with a large degree of spin polarization, or just many electrons with a small degree of spin polarization. For this reason, we focus more on the degree of spin polarization (DSP), which is intuitively easier to understand than ζ^{xyz}.

In Fig. 3, we plot the degree of spin polarization $DSP^z(\omega)$. Because of the relatively high symmetry of GaAs, the exact crystal cut is unimportant; the injected spin density will always be aligned parallel or antiparallel to the laser beam. In Fig. 3, we also plot the degree of spin without the coherence terms. We see that the coherence terms account for more than 70% of the total spectrum in this calculation, and neglecting them leads to unphysical results.

We see that the $DSP(\omega)$ calculated with the LDA is quantitatively the same as the spectrum calculated with the $\mathbf{k} \cdot \mathbf{p}$ method up to about 2.5 eV. The differences between the methods, shown in the $\xi^{xx}(\omega)$ and $\zeta^{xyz}(\omega)$ spectra, tend to cancel out. That is, the errors are relative and do not affect the $DSP(\omega)$. This is somewhat fortuitous in GaAs, since the participating conduction bands are well separated from other bands and the injected spin polarization is thus highly dependent on the crystal symmetry and less on the details of the band structure.

The degree of spin polarization near the band edge is 50%. This result is easily understood by considering the en-
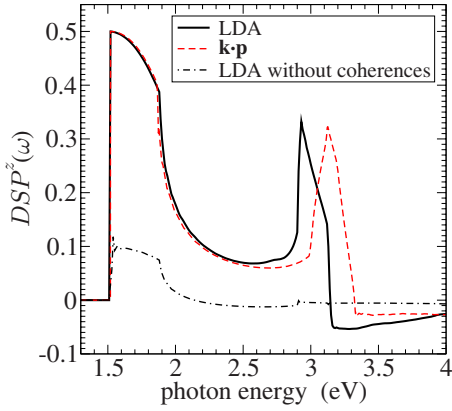
FIG. 3. (Color online) Comparison of the degree of spin polarization injected calculated using LDA (solid black line) and **k·p** (dashed red line) band structures. The differences in the calculated spectra for $\xi^{xx}(\omega)$ (Fig. 1) and $\zeta^{xyz}(\omega)$ spectra (Fig. 2) have canceled to give very similar results for $DSP^z(\omega)$ up to about 2.5 eV. The dash-dotted line is the degree of spin polarization calculated using Eq. (4) and shows that neglecting the coherences can lead to an incorrect spectrum.

ergy level diagram of the GaAs states around the Γ point shown in Fig. 4. We review this well-known model here to emphasize its limitations and strengths when we use the analogous model to understand the spin-injection rates in Si and CdSe in the following sections. Assuming as usual that the $\hat{z}$ axis is the quantization direction, for the spin states, we will use the shorthand $|+\rangle$ for spin up and $|-\rangle$ for spin down. The six highest-energy valence band states of GaAs are p-like, and in the absence of spin-orbit coupling, these six states would be degenerate. The effect of spin-orbit coupling is to split the p states into four degenerate $j=3/2$ states, which form the highest-energy valence states, and two $j=1/2$ states, whose energy is lowered by the split-off energy amount. The orbital parts of the states are denoted by $|11\rangle$, $|10\rangle$, and $|1\bar{1}\rangle$. The two heavy-hole states take the form

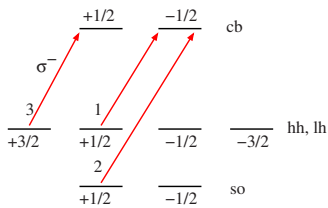$$\left| \frac{3}{2}, \frac{3}{2} \right\rangle = |11\rangle | + \rangle, \tag{24}$$

FIG. 4. (Color online) Energy levels at the Γ point for bulk GaAs. The highest six valence states ($J=3/2$) and lowest two conduction states ($J=1/2$) are shown. Underneath each state level line is its corresponding j_z. The six valence bands are classified into heavy-hole (hh), light-hole (lh), and split-off (so) bands. The arrows denote allowed transitions with σ^- polarized light. The numbers next to the arrows represent transition strengths relative to the other transitions at that photon energy.

$$\left| \frac{3}{2}, -\frac{3}{2} \right\rangle = |1\bar{1}\rangle | - \rangle, \tag{25}$$

and the two light-hole states take the form

$$\left| \frac{3}{2}, \frac{1}{2} \right\rangle = \sqrt{\frac{2}{3}} |10\rangle | + \rangle + \sqrt{\frac{1}{3}} |11\rangle | - \rangle, \tag{26}$$

$$\left| \frac{3}{2}, -\frac{1}{2} \right\rangle = \sqrt{\frac{1}{3}} |1\bar{1}\rangle | + \rangle + \sqrt{\frac{2}{3}} |10\rangle | - \rangle. \tag{27}$$

The conduction band states are s-like, and at the Γ point, there are two degenerate $j=1/2$ states, which, in an obvious notation, take the form

$$\left| \frac{1}{2}, \frac{1}{2} \right\rangle = |00\rangle | + \rangle,$$

$$\left| \frac{1}{2}, -\frac{1}{2} \right\rangle = |00\rangle | - \rangle.$$

Band-edge absorption excites electrons from the four $j=3/2$ valence states to the two $j=1/2$ conduction states. The selection rules limit the allowed transitions for circularly polarized light. The absorption of left-circularly polarized (σ^- if propagating in the $-\hat{z}$ direction) photons excites only from valence states $j_z=3/2$ and $j_z=1/2$ to the conduction states, in a 3:1 ratio, respectively, as depicted in Fig. 4. From Eq. (14), this leads to a degree of spin polarization from excitation of σ^- polarized light of

$$DSP = \frac{\dot{S}_{+1/2} + \dot{S}_{-1/2}}{(\hbar/2)(\dot{n}_{+1/2} + \dot{n}_{-1/2})} = \frac{3\left(\frac{\hbar}{2}\right) + 1\left(-\frac{\hbar}{2}\right)}{(\hbar/2)(3+1)} = \frac{1}{2}, \tag{28}$$

a 50% net polarization of the conduction electrons. The split-off states are two $j=1/2$ states. Absorption of circularly polarized light, exciting electrons from these states to the lowest conduction bands, gives 100% spin-polarized electrons in the conduction band. The spin of these electrons is opposite in direction to the net spin of the electrons excited by the same polarization at the band edge.

One limitation of this atomiclike model (Fig. 4) arises when we try to decompose the $\zeta^{xyz}(\omega)$ spectrum into contributions from the different valence bands. For photon energies that move the absorption away from Γ, the heavy-hole band is no longer degenerate with the light hole. So, from the model in Fig. 4, one might expect the $j_z=\pm 3/2$ states to split from the $j_z=\pm 1/2$ states and for the transitions from these states to lead to opposite spin polarizations. In Fig. 5, we identify the contributions to $\zeta^{xyz}(\omega)$ from the heavy-hole (hh), light-hole (lh) and split-off band (so) bands. Each line in Fig. 5 includes a sum over the quasidegenerate states. From the figure, it is clear that near the band edge, both the heavy-hole and light-hole transitions contribute spins in the same direction, as is well known.[1] This can be understood from the model by first noting that the identification of the $j_z=\pm 3/2$ as heavy-hole states, and the $j_z=\pm 1/2$ as light-hole
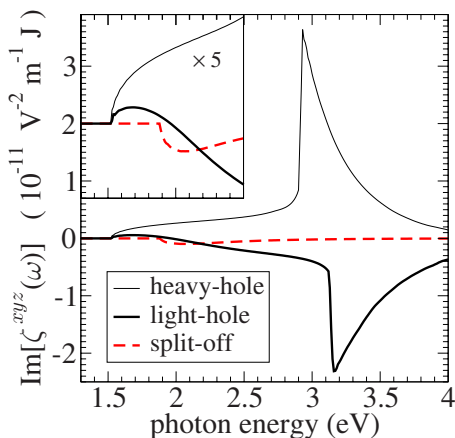
FIG. 5. (Color online) Contributions to the total electron spin-injection for transitions from the heavy-hole (thin black line), light-hole (thick black line), and split-off (dashed red line) bands calculated with the pseudopotential method. The inset shows the same spectra multiplied by 5 and shifted up. The inset shares the same energy axis as the larger frame. Note the sign change in the contribution from the light-hole band.

states, literally applies to states only along k_z. Along an arbitrary direction $\hat{\mathbf{k}}$, the Luttinger-Kohn Hamiltonian H_{LK} can be used to describe the highest valence bands in GaAs near Γ. In the spherical approximation, which neglects the spin splitting, it takes the form,

$$H_{LK} = \frac{\hbar^2 k^2}{2m}\left(\gamma_1 + \frac{5}{2}\gamma_2\right) - \frac{\hbar^2}{m}\gamma_2(\mathbf{k}\cdot\mathbf{J})^2,$$

where γ_1 and γ_2 are material dependent parameters, and $\mathbf{J}$ is the spin-3/2 operator. It is then found that the $j_{\hat{\mathbf{k}}}=\pm 3/2$ states [denoted $|\frac{3}{2},\pm\frac{3}{2}(\hat{\mathbf{k}})\rangle$] comprise the heavy-hole bands and that the $j_{\hat{\mathbf{k}}}=\pm 1/2$ states [denoted $|\frac{3}{2},\pm\frac{1}{2}(\hat{\mathbf{k}})\rangle$] comprise the light-hole bands. At transition energies away from Γ, averaging over the sphere of $\mathbf{k}$ that contributes to the injection, using

$$\int \frac{d\hat{\mathbf{k}}}{4\pi}|jm(\hat{\mathbf{k}})\rangle\langle jm(\hat{\mathbf{k}})| = \frac{1}{2j+1}\sum_{m'}|jm'\rangle\langle jm'|,$$

shows that the degrees of spin polarization along $\hat{z}$ due to absorption from the heavy-hole bands and the light-hole bands are both 50%.

In Fig. 6, we show the degree of spin polarization for the separate transitions (heavy hole, light hole, and split off). We have taken the spin-injection rate for each transition and divided it by the injection rate for that transition. We see that the electrons from the split-off transitions are, on average, oppositely spin polarized from the electrons from the heavy-hole transitions. However, although the electrons from the split-off band are highly polarized, Fig. 5 shows that there are so few of them compared to the number from the heavy-hole and light-hole bands that they make a small contribution to the overall DSP (see Fig. 3).
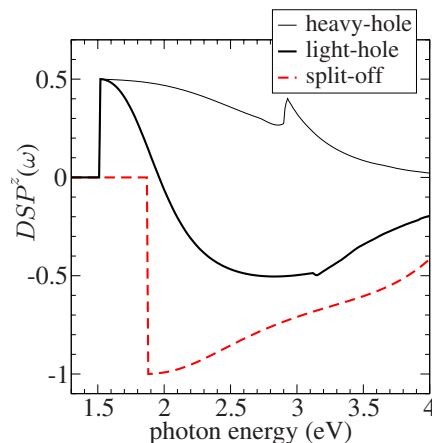

FIG. 6. (Color online) Degree of spin polarization associated with different transitions calculated with the pseudopotential method. The electrons excited into the lowest conduction band via transitions from the heavy-hole (thin black line) and light-hole (thick black line) bands are 50% spin polarized near the band edge, but the electrons from the heavy-hole bands are significantly polarized for a wide range of photon energies. The electrons excited from the split-off (dashed red line) band are 100% spin polarized near the band edge.

At energies above the 350 meV split-off energy ($\hbar\omega > 1.86$ eV), the injected spin density drops. One might think the drop is caused by transitions from the split-off band, but the drop in spin polarization is actually from the light-hole band transitions. Even though near Γ the transitions from the heavy-hole and light-hole bands contribute in a reinforcing manner, this is not the case at energies where the split-off band transitions are important. At these energies, the light-hole band can no longer be approximated by its Γ-point state. The inset of Fig. 5 shows that at energies where absorption from the split-off band can occur, the transitions from the light-hole band have a large effect in reducing the total spin-injection.

The degree of spin polarization from optical orientation in GaAs has been probed by various techniques. Photoluminescence experiments rely on the circular polarization of the emitted light when spin-polarized electrons recombine with holes.[1,41] In Faraday rotation experiments, the rotation of the polarization plane of a linear polarized beam transmitted through the material is measured.[42,43] Pump-probe experiments, which excite with one circular polarization and probe with both left and right polarizations, can also be used to measure the spin densities.[44] In these measurements of optical orientation, photons with energies just above the band gap were used for practical reasons. Our calculations show that at higher energies, well above the split-off energy, there is another excitation regime where a strong degree of spin polarization is induced. Figure 3 shows that at 3 eV, a roughly 25% degree of spin polarization is expected. This polarization comes from splitting of the heavy-hole and light-hole bands in the Γ-L valley. We know of no experiment on optical orientation that directly probes the spin of electrons in the band at this energy. However, related to experiments on optical orientation is a group of experiments on

spin-polarized photoionization in GaAs.[45,46] In these experiments, circularly polarized light is used to photoionize electrons from a GaAs sample. As expected, the electrons excited in these experiments are spin polarized, but the feature is that the electrons keep a substantial amount of their spin polarization even after photoionization. In these experiments, where photons with energies between 1.5 and 4 eV were used, it was found that in the region around 3 eV photon energy, the ionized electrons had a spin polarization of up to 10%.[45] Figures 6 and 8 of Pierce and Meier[45] show the spin polarization measured in their experiments as a function of photon energy. Although these spectra show qualitative features similar to our spin polarization spectra in Fig. 3, a quantitative comparison would require a detailed analysis of the ionization process to extract the degree of spin polarization optically injected.

B. Si

We now turn to spin-injection rates in bulk silicon. Both theoretically and experimentally, this has been studied much less than spin-injection in GaAs and other III-V semiconductors. We are unaware of any direct measurements of electron spin optical orientation in bulk Si. However, measurements of the nuclear spin polarization of ^{29}Si, induced by the hyperfine interaction with the optically injected electron spins, have indirectly probed the optical orientation. These studies were first reported by Lampel[10] and then extended by Bagraev *et al.*[47] Recently, Verhulst *et al.*[48,49] have revisited the study of electron spins in Si in the context of quantum computing. The electron spin density created in these experiments arises from indirect excitation with circularly polarized light, where a phonon provides the necessary crystal momentum for the absorption above the indirect band gap. Even though the indirect absorption process has been thoroughly studied for linearly polarized light, spin-injection arising from the indirect absorption of circularly polarized light has not. The difficulty in directly measuring the electron spins in the conduction band using photoluminescence arises because the lifetime of the electrons in the side valleys is larger than the spin lifetime;[2] the spin has predominantly decayed by the time the electrons and holes recombine, and so the luminescence is unpolarized. Nonetheless, Roux *et al.*[50] have recently reported a measurement of 5% polarization of the photoluminescence from this recombination.

In the analysis of their experiments, these groups assumed that the phonon transitions do not affect the spin properties of the electron, so that the final states in the conduction band near the X valleys have the same spin as the intermediate virtual state at the Γ point. We will also not address the indirect process here but instead focus on absorption across the direct gap, which is a physically simpler process and should dominate at high enough photon energies and low enough temperatures. The direct band gap is large, roughly 3.4 eV, but it is still within the optical regime.

Unlike GaAs, Si is centrosymmetric. Because of this, there is no spin splitting in the band structure and every k state is doubly degenerate, so there are no coherences excited. However, the spin-orbit interaction does complicate
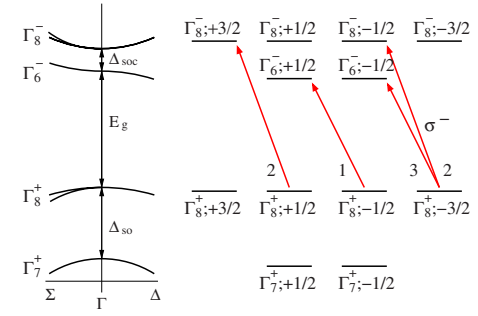

FIG. 7. (Color online) On the left hand side, we sketch the bands around Γ for bulk Si. On the right hand side, we indicate the energy levels at the Γ point along with the notation used in the text. The arrows indicate the allowed transitions at the band edge that we consider in the text, and the numbers adjacent each arrow give the relative strength of that transition.

the band structure at the zone center. Although our calculations apply to the entire Brillouin zone, the region around the Γ point will be our focus. Before we discuss the spin-injection rate away from the Γ point, we will revisit the problem of excitation directly at Γ. The zone center bands are depicted in Fig. 7. Silicon belongs to the O_h point group. Without spin-orbit coupling, the lowest conduction bands at Γ belong to the Γ_{15} representation (with basis functions that transform like $\{x, y, z\}$ under the point group operations), and the highest valence states belong to the irreducible representation Γ'_{25} (with basis functions that transform as $\{xy, yz, zx\}$, which we label as $\{Z, X, Y\}$). With spin-orbit coupling, both the valence bands and conduction bands exhibit spin-orbit splitting. The valence band split-off energy has been thoroughly studied and is well known to be 44 meV. However, the splitting in the conduction bands Δ_{soc} is a little smaller, and not much attention has been focused on it; these conduction states do not participate in typical Si experiments, which focus on electrons in the X valleys. In our LDA calculations, we find that this splitting is 32 meV. In the double group notation, the heavy- and light-valence states belong to Γ_8^+ and are given by

$$\left| \Gamma_8^+; \frac{3}{2} \right\rangle = -\frac{1}{\sqrt{2}} |X + iY\rangle | \uparrow \rangle, \qquad (29)$$

$$\left| \Gamma_8^+; \frac{1}{2} \right\rangle = \sqrt{\frac{2}{3}} |Z\rangle | \uparrow \rangle - \frac{1}{\sqrt{6}} |X + iY\rangle | \downarrow \rangle, \qquad (30)$$

$$\left| \Gamma_8^+; -\frac{1}{2} \right\rangle = \frac{1}{\sqrt{6}} |X - iY\rangle | \uparrow \rangle + \sqrt{\frac{2}{3}} |Z\rangle | \downarrow \rangle, \qquad (31)$$

$$\left| \Gamma_8^+; -\frac{3}{2} \right\rangle = \frac{1}{\sqrt{2}} |X - iY\rangle | \downarrow \rangle. \qquad (32)$$

The split-off valence band belongs to Γ_7^+. Transitions from it are very weak, and so this band will not play an important role in this discussion. Turning to the conduction bands, the

split-off conduction bands are lower in energy and belong to Γ_6^-. We can write these states as

$$\left|\Gamma_6^-; +\frac{1}{2}\right\rangle = \frac{1}{\sqrt{3}}|z\rangle|+\rangle + \frac{1}{\sqrt{3}}|x+iy\rangle|-\rangle, \qquad (33)$$

$$\left|\Gamma_6^-; -\frac{1}{2}\right\rangle = \frac{1}{\sqrt{3}}|x-iy\rangle|+\rangle - \frac{1}{\sqrt{3}}|z\rangle|-\rangle. \qquad (34)$$

The four other bands belong to Γ_8^-. They are given by

$$\left|\Gamma_8^-; +\frac{3}{2}\right\rangle = -\frac{1}{\sqrt{2}}|x+iy\rangle|+\rangle, \qquad (35)$$

$$\left|\Gamma_8^-; +\frac{1}{2}\right\rangle = \sqrt{\frac{2}{3}}|z\rangle|+\rangle - \sqrt{\frac{1}{6}}|x+iy\rangle|-\rangle, \qquad (36)$$

$$\left|\Gamma_8^-; -\frac{1}{2}\right\rangle = \sqrt{\frac{1}{6}}|x-iy\rangle|+\rangle + \sqrt{\frac{2}{3}}|z\rangle|-\rangle. \qquad (37)$$

$$\left|\Gamma_8^-; -\frac{3}{2}\right\rangle = \frac{1}{\sqrt{2}}|x-iy\rangle|-\rangle, \qquad (38)$$

These bands are degenerate along the high symmetry lines Δ and Λ not shown in Fig. 7.

In the right hand side of the Fig. 7, we show the allowed transitions near the Γ point for σ^- circular polarization. The states are labeled by j_z in the conduction band and by $\langle j_z \rangle$ in the valence band. Unlike GaAs, the valence states are not eigenstates of j_z. For photon energies just crossing the band gap (E_g), only transitions from the $\langle j_z \rangle = +1/2$ and $\langle j_z \rangle = -3/2$ states are allowed. In the context of the 30-band model, a single parameter Q describes the relevant matrix elements for these transitions: $\langle x|p^y|Z\rangle = \langle y|p^z|X\rangle = \langle z|p^x|Y\rangle = \langle y|p^x|Z\rangle = \langle z|p^y|X\rangle = \langle x|p^z|Y\rangle = imQ/\hbar$. For matrix elements connecting the valence states to the lowest conduction states, we have, for example,

$$\left\langle \Gamma_6^-; -\frac{1}{2}\right|\mathbf{p}\left|\Gamma_8^+; -\frac{3}{2}\right\rangle = \frac{1}{\sqrt{3}}\frac{mQ}{\hbar}\frac{(\hat{\mathbf{x}}+i\hat{\mathbf{y}})}{\sqrt{2}} \qquad (39)$$

and

$$\left\langle \Gamma_6^-; +\frac{1}{2}\right|\mathbf{p}\left|\Gamma_8^+; +\frac{1}{2}\right\rangle = \frac{mQ}{\hbar}\frac{(\hat{\mathbf{x}}+i\hat{\mathbf{y}})}{\sqrt{2}}, \qquad (40)$$

which connect to σ^- light. These are the only nonzero transitions, for excitation just at the band edge, and these are excited in a 3:1 ratio. The expectations of spin in the $|\Gamma_6^-; -\frac{1}{2}\rangle$ and $|\Gamma_6^-; +\frac{1}{2}\rangle$ states are $\frac{1}{3}\frac{\hbar}{2}$ and $-\frac{1}{3}\frac{\hbar}{2}$, respectively. This gives a net DSP of

$$\text{DSP} = \frac{\dot{S}_{\Gamma_6^-;1/2} + \dot{S}_{\Gamma_6^-;-1/2}}{(\hbar/2)(\dot{n}_{\Gamma_6^-;1/2} + \dot{n}_{\Gamma_6^-;-1/2})} = \frac{3\left(-\frac{\hbar}{6}\right) + 1\left(\frac{\hbar}{6}\right)}{(\hbar/2)(3+1)} = -\frac{1}{6}. \qquad (41)$$

If the spin-orbit splitting in the conduction band were neglected, the six conduction states would be degenerate. We

could choose them to be $|I\rangle|\pm\rangle$, where $I = x, y, z$. For σ^- light, this gives a DSP of -25%. We note that this is in disagreement with the result of Lampel, who found instead that excitation with σ^+ polarized light gives a DSP of -25%.[48,51]

Note that the matrix elements sketched in Fig. 7 seem counterintuitive, at least by the kind of argument often made for the matrix elements sketched in Fig. 4 for GaAs. As an example, consider the stronger transition in that simpler GaAs diagram. One can envision a σ^- photon with angular momentum $-\hbar\hat{\mathbf{z}}$ being absorbed as it creates a hole with angular momentum $-\frac{3}{2}\hbar\hat{\mathbf{z}}$ and an electron with angular momentum $\frac{1}{2}\hbar\hat{\mathbf{z}}$, thus conserving angular momentum in analogy with the corresponding transitions in atomic physics. In Fig. 7, however, the transitions seem to go "in the wrong way," and this simple kind of picture fails. However, it is important to realize that the Γ_8^+ states in Si, together with the Γ_7^+ states, form six states that are split by the crystal field from another four states. Together, these ten states, in the absence of either crystal field or spin-orbit splitting, would have orbital components that would transform under (proper and improper) rotations as would atomic d states. The strong crystal-field splitting involves the lattice as a possible source or sink of angular momentum in any transition, and the kind of atomic picture based on conservation of angular momentum so useful as a heuristic to understand Fig. 4 is simply not relevant for transitions we have just discussed in Si.

At higher energies, there is mixing of the states, and so we cannot analytically determine the spin-injection rate, either with or without the spin-orbit coupling in the conduction bands. For σ^- polarized excitation, the carrier injection and spin-injection rates take the forms given by given by Eqs. (20) and (23), respectively, as they are for GaAs. To help appreciate the differences between a **k·p** and a LDA band structure calculation, we again compare the spin-injection rate and DSP calculated from these two methods. In the LDA calculations, we find a theoretical lattice constant of $10.17a_0$ and that the lowest direct energy transitions occur at the Γ point as expected. However, in the **k·p** calculations, we find that the minimum direct energy transition occurs away from the Γ point, in a direction $15°$ off X toward W, about 20% of the distance to the BZ edge. The band gap at this point is about 45 meV lower then the energy gap at Γ. To correct the LDA band gap, we use a scissor shift that sets the LDA Γ-point energy gap to the **k·p** Γ-point energy gap (3.40 eV). We make this choice to help compare the two methods: the transitions at the Γ point will then have the same transition energies as well as the same spin. As in our other LDA calculations, where a different scissor shift is used, perhaps to set the indirect band gap energy instead of the direct gap energy, the only difference to the LDA spectra would be an overall shift in energy.

In Fig. 8, we plot $\zeta^{xyz}(\omega)$ for bulk Si, calculated with both LDA and **k·p** band structures. We see that the LDA and **k·p** results are not as similar as they were for GaAs; indeed, for Si, they are qualitatively different. We plot the DSP in Fig. 9, again for σ^- polarized light. Unlike for GaAs, where the differences in the LDA and **k·p** calculations of $\zeta^{xyz}(\omega)$ and $\xi^{xx}(\omega)$ largely cancel out to give very similar results for DSP(ω), for Si, the two methods give dissimilar results.
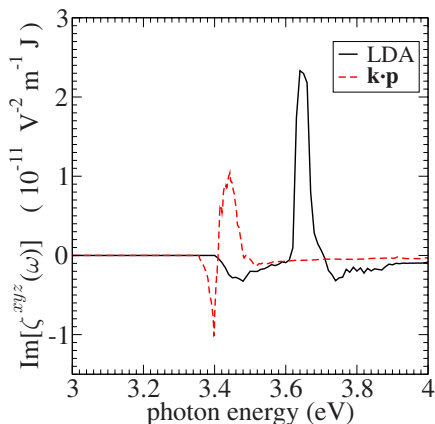
FIG. 8. (Color online) A comparison of the spin-injection tensor component ζ^{xyz} for bulk Si calculated with the $\mathbf{k}\cdot\mathbf{p}$ (dashed red line) and LDA (solid black line) band structures. Note that here, they are significantly different, where as in GaAs, they are qualitatively the same.

There are two reasons for the disagreement between the $\mathbf{k}\cdot\mathbf{p}$ and LDA result, and they are both associated with the $\mathbf{k}\cdot\mathbf{p}$ treatment of the conduction split-off band. First, in the $\mathbf{k}\cdot\mathbf{p}$ model of Richard *et al.*,[8] the split-off energy of the conduction states is set to zero. This decreases the energy width of the states participating in the absorption and narrows its spectral range. If we add into the model this split-off energy, by hand, we find that the $\mathbf{k}\cdot\mathbf{p}$ spectrum moves closer to the LDA spectrum. However, there are still significant differences, due to a second reason.

The LDA bands, which exhibit a direct gap at Γ and include the conduction band spin-orbit splitting there, lead to a maximum degree of spin polarization near the onset of absorption of roughly -30%. In the $\mathbf{k}\cdot\mathbf{p}$ calculation, where the direct gap is not at the Γ point, it is the off-zone-center states that contribute near the onset of absorption. These states do not exhibit the high symmetry of Γ and this leads to a degree of spin polarization closer to -5%.
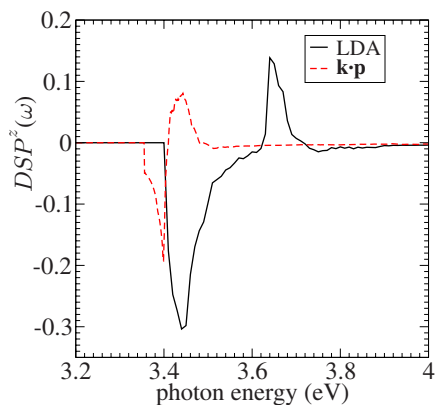

FIG. 9. (Color online) The degree of spin polarization injected into bulk Si with circularly polarized light, calculated with both the LDA (solid black line) and a $\mathbf{k}\cdot\mathbf{p}$ (dashed red line) method. The maximum spin polarization predicted by the LDA is roughly -30%, whereas the $\mathbf{k}\cdot\mathbf{p}$ method gives roughly -20%.
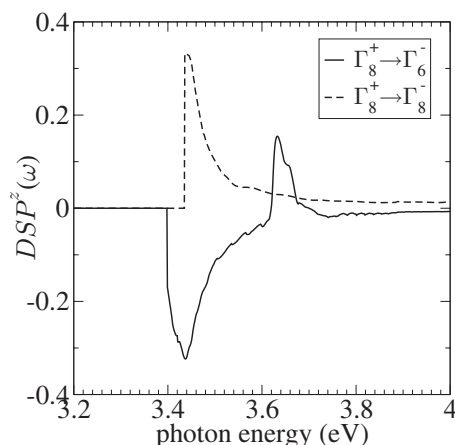

FIG. 10. Breakdown of the degree of spin polarization into different band contributions, calculated with the LDA. The states are identified in Fig. 7. The Γ_8^+ to Γ_6^- transitions occur at the band edge and involve the highest valence bands with a split-off-like conduction band. The other transitions, from Γ_7^+, make a small contribution to the total spin-injection rate so they are excluded here.

To see the contribution of the Γ point in our $\mathbf{k}\cdot\mathbf{p}$ calculation of direct absorption, one has to move up to a photon energy of 3.40 eV, which can connect the top of the valence band at Γ with the conduction bands there. At that energy, the $\mathbf{k}\cdot\mathbf{p}$ calculation predicts a spin polarization of roughly -20%. It would give -25% if only the region around the Γ point were contributing, but because this is not the minimum transition energy in this calculation, there are transitions occurring at other points in the BZ. These extra transitions mask the high symmetry Γ-point transitions, and so one does not see a "pure" signal.

Returning to the LDA calculation, with its direct gap at Γ where conduction spin-orbit splitting is present, careful inspection of the LDA curve in Fig. 9 reveals that at the onset of absorption (3.40 eV), the spin-injection rate is actually -16.7% spin polarized, in agreement with the analysis leading up to Eq. (41). From there it then increases to roughly -30% for photon energies of 3.45 eV. We expect that the LDA gives a better approximation to reality than the $\mathbf{k}\cdot\mathbf{p}$ model, at least with the parameters we have used here, since the latter neglects spin-orbit coupling in the conduction band and incorrectly reproduces the location of the minimum direct energy gap.

The spin-injection rate from the different transitions in our LDA calculation can be seen more clearly in Fig. 10, where we show the DSP from the individual transitions. We only show the transitions that have the most effect on the net spin-injection rate; the transitions from the split-off band are very weak so they are excluded here. The transitions from Γ_8^+ to Γ_6^- show the $-1/6$ polarization more clearly. At slightly higher energy, the transitions from Γ_8^+ to Γ_7^- kick in, with a polarization of $+1/3$, which gradually diminishes at higher photon energies. The $+1/3$ spin polarization at the band edge can be analytically verified by considering the states in Eqs. (29)–(32) and (35)–(38).

At photon energies above 3.7 eV, there is no significant spin injection. The small energy window is because of the

weak spin-orbit interaction. Thus, any experimental investigation into the spin properties of the direct optical transitions must be done with a precisely tuned laser. However, indirect absorption involves the excitation of virtual conduction states, and so the spin-injection into these states can still be significant.

C. CdSe

Finally, we consider the optical spin-injection rate in bulk *wurtzite* CdSe. The wurtzite semiconductors are direct gap, noncentrosymmetric binary compounds, as are the zinc-blende semiconductors, but wurtzite belongs to the hexagonal crystal system; it is less symmetric than zinc blende and has a more complicated primitive cell. In particular, its primitive cell consists of four atoms instead of two. The orientation of the crystal is important in understanding the response. We use the coordinate system and basis convention as laid out in Grosso and Parravacini.[52] The primitive lattice vectors are $\mathbf{t}_1 = a(1/2, \sqrt{3}/2, 0)$, $\mathbf{t}_2 = a(-1/2, \sqrt{3}/2, 0)$, and $\mathbf{t}_3 = c(0, 0, 1)$. The direction of $\mathbf{t}_3$ is called the c axis and is typically the growth axis. We use the empirical values $a = 8.126a_0$ and $c = 13.24a_0$. The Cd atoms are set at $(0, 0, 0)$ and $(0, a/\sqrt{3}, c/2)$, and the Se atoms are at $(0, 0, uc)$ and $(0, a/\sqrt{3}, uc + c/2)$. For the internal parameter u, we use the ideal value $u = 3/8$. We use the HGH pseudopotentials and treat the cation Cd semicore $4d$ states as core electrons. This is sufficient if we are interested in only the states near the band edges. To accurately study the higher-energy excitations, one would need to use a pseudopotential that treats the semicore states as valence states, or an all-electron method. The LDA band gap is found to be 0.765 eV, and we use a scissors correction to raise it to the experimental value of 1.75 eV.

The hexagonal structure of CdSe leads to a crystal-field splitting which splits the heavy-hole and light-hole bands at the zone center. Another consequence of the crystal-field splitting is that the energy of the split-off band is further lowered.[53] The complexity of the electronic structure in wurtzite materials leads to complicated $\mathbf{k} \cdot \mathbf{p}$ methods. Unlike for Si and GaAs, we know of no full-band structure $\mathbf{k} \cdot \mathbf{p}$ method for CdSe or any other wurtzite material. There are well understood models available for near the Γ point,[53–55] but for brevity, we do not reproduce them here, since our emphasis is on full-zone calculations.

For the hexagonal structure, the absorption tensor $\xi^{ab}(\omega)$ is diagonal in the frame used to identify the $\mathbf{t}_i$ above, but the low symmetry leads to $\xi^{xx}(\omega) = \xi^{yy}(\omega) \neq \xi^{zz}(\omega)$. For the spin-injection rate, the only nonzero components are $\zeta^{xyz}(\omega)$ and components associated with all the permutations of x, y, and z. However, now we have $\zeta^{zxy}(\omega) \neq \zeta^{xyz}(\omega)$, etc. The lack of symmetry indicates that the spin-injection process can be quite different for different orientations of the crystal.

We will consider two crystal orientations and consider excitation by circularly polarized light. In the first orientation, the light propagates in the $-\hat{\mathbf{z}}$ direction. Here, the laser electric field is polarized in the xy plane [Eq. (19)], and only the components $\zeta^{zxy}(\omega) = -\zeta^{zyx}(\omega)$ are accessed for spin-injection. The spin-injection rate in this case is given by
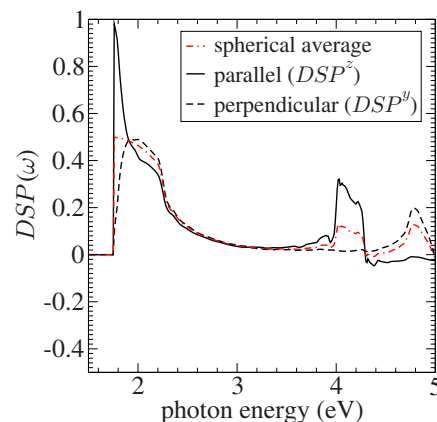

FIG. 11. (Color online) Degree of optically injected spin polarization in CdSe for two different crystal orientations. The solid black line is the spectrum for the orientation with the crystal c axis aligned parallel to the direction of light propagation, and the dashed red line is for the crystal c axis aligned perpendicular to direction of light propagation. The dash-dotted red line is the degree of spin polarization for an ensemble of randomly oriented crystals, as described in the text.

$$\dot{S}^z = \text{Im}[\zeta^{zxy}(\omega)]|E_0|^2. \qquad (42)$$

In the second orientation, the c axis is perpendicular to the direction of light propagation, which is along $-\hat{\mathbf{y}}$ so that the field polarization is given by $\mathbf{E}(\omega) = E_0(\hat{\mathbf{z}} - i\hat{\mathbf{x}})/\sqrt{2}$. The spin-injection rate is given by

$$\dot{S}^y = \text{Im}[\zeta^{yzx}(\omega)]|E_0|^2. \qquad (43)$$

Here, it is the components $\zeta^{yzx}(\omega) = \zeta^{xyz}(\omega) = -\zeta^{yxz}(\omega) = -\zeta^{xzy}(\omega)$ that are accessed; as long as we are interested in bulk spins and not surface effects, the same DSP results for any orientation of the crystal where the c axis is perpendicular to the direction of light propagation. In Fig. 11, we plot the degree of spin polarization of optically injected electrons in CdSe for these two crystal orientations. The spectrum for the first ("parallel") orientation is represented by the solid line, and the second ("perpendicular") orientation is represented by the dashed line.

The two spectra in Fig. 11 are quite different for energies just above the band edge, up to around 2.2 eV. In the parallel orientation, we see that almost 100% polarized spin-injection is achieved for photon energies just at the band gap. This is a consequence of the crystal-field splitting. The heavy-hole and light-hole bands are split, and excitation from only the heavy-hole band occurs at the band edge. Unlike in bulk GaAs, averaging over a small sphere around Γ does not result in spin-injection from the heavy-hole band that is 50% polarized, since the crystal-field splitting causes the heavy-hole states to be $j_z = \pm 3/2$ states, and the light-hole states to be $j_z = \pm 1/2$ states. For photons with energy just above the crystal-field splitting energy (39 meV in this calculation), the spectrum drops to roughly 50%. At these energies, the excitation occurs from the heavy-hole and light-hole states. Moreover, there is strong mixing of the Γ-point states, and so

the excitation is analogous to that of GaAs at the band edge. For the perpendicular orientation, the degree of spin polarization starts at zero at the band edge and, as the energy is increased, rises to 50%. Here, the absorption of circularly polarized light is forbidden just above the band edge, but at slightly higher energies, the valence states are combinations of zone center heavy-hole and light-hole states, and circularly polarized light can be absorbed. Since the states are $j = 3/2$ combinations of p states, there is a maximum degree of spin polarization of 50%, again analogous to GaAs. For photon energies at and just above 2.2 eV, the valence states contain mixing from the zone center split-off states and, yet again as in GaAs, the DSP drops off rapidly for both orientations. For photon energies between 2.5 and 4.0 eV, the degree of spin polarization is very low and nearly equal in both cases. However, at energies right above this range, the degree of spin polarization is quite different for the two orientations. At around 4.1 eV, a 30% polarization is found in the parallel orientation, and at 4.8 eV, a 20% polarization in the perpendicular orientation. This excitation occurs near zone boundaries in the BZ. Even though the energies required to probe these interesting transitions are too high for usual optical methods, we include them to show how asymmetric these two orientations are at these energies.

We are unaware of any experimental study measuring the spin polarization of optically injected electrons in bulk CdSe, or any bulk wurtzite crystal. However, studies of exciton spin-injection in various wurtzite nanocrystals have been reported.[56–59] Most optical experiments in bulk wurtzite, including those probing effects not relying on spin-orbit coupling, are done with the sample oriented such that the sixfold symmetric axis (the c axis) is parallel to the laser beam propagation. This orientation is chosen because the selection rules allow for transitions from the heavy-hole band at the zone center, and because the surface in this orientation is typically cleaner than in the perpendicular orientation. In many experiments involving nanocrystals, however, the nanocrystals are randomly oriented throughout a solution. If the nanocrystals are large enough that the bulk wurtzite symmetries hold, the effective spin-injection rate tensor $\boldsymbol{\zeta}_{\text{eff}}(\omega)$ and carrier injection rate tensor $\boldsymbol{\zeta}_{\text{eff}}(\omega)$ for such an ensemble can be found by averaging the bulk tensors $\boldsymbol{\zeta}(\omega)$ and $\boldsymbol{\xi}(\omega)$ over all orientations. This gives $\xi_{\text{eff}}^{xx}(\omega) = [\xi^{zz}(\omega) + 2\xi^{xx}(\omega)]/3$ and $\zeta_{\text{eff}}^{zxy}(\omega) = [\zeta^{zxy}(\omega) + 2\zeta^{yzx}(\omega)]/3$. The other tensor components $\xi_{\text{eff}}^{ab}(\omega)$ and $\zeta_{\text{eff}}^{abc}(\omega)$ satisfy the cubic symmetries in Eqs. (21) and (22). The resulting average degree of spin polarization for such an ensemble of randomly oriented crystals is given by the dash-dotted red line in Fig. 11. Band-edge excitation in this case gives 50% spin polarization, as in the cubic crystals.

band model may not exist. The injected degree of spin polarization has been calculated for photon energies up to 4 eV. For GaAs and Si, we have compared the results with those from a 30-band $\mathbf{k} \cdot \mathbf{p}$ model. For GaAs, we have found good agreement between the *ab initio* and the $\mathbf{k} \cdot \mathbf{p}$ results. Especially for the degree of spin polarization, this is partly due to a fortuitous cancellation of errors. Both models predict a large degree of spin polarization at high photon energies near 3.2 eV. Although this spin-injection has not been directly measured with the usual techniques for measuring optical orientation, indirect experimental evidence for this exists in spin-polarized photoemission experiments. For Si, we find that within a small energy window above the direct gap, a spin polarization of up to 30% can be injected. We also found that the spin-injection predicted from different models agreed less than for GaAs. This is because the spin-injection is due to a small region of the Brillouin zone and is sensitive to the details there. For the band-edge absorption, both pseudopotential and $\mathbf{k} \cdot \mathbf{p}$ calculations disagree with a simple atomic picture which predicts a band-edge spin polarization of −25%.[48,51] The pseudopotential band structure calculation predicts a degree of spin polarization of −16%. The differences can be traced back to two factors: the spin-orbit splitting in the conduction band and the position of the direct band gap minimum. Both the $\mathbf{k} \cdot \mathbf{p}$ model and the simple atomic model exclude the small spin-orbit splitting in the lowest conduction states. With this splitting included, the symmetry of the states are altered such as to cause the band-edge degree of spin polarization to change from −25% (assuming no splitting) to −16%. Additionally, in the 30-band $\mathbf{k} \cdot \mathbf{p}$ model we find that the lowest-energy direct transitions in Si occur away from the Γ point. This further complicates the band-edge structure and changes the degree of spin polarization away from −25%. As a more complicated example, we calculate the spin-injection rate in CdSe. We verify the known result that nearly 100% spin polarization can be injected for orientations with the c axis parallel to the light beam propagation. For orientations where the c axis is orthogonal to the light beam propagation, we find that up to 50% spin polarization can be injected. For both orientations, we show that significant spin polarization is expected at higher photon energies.

To efficiently calculate the spectra, we have developed an adaptive Brillouin zone integration method. The scheme lets us refine the $\mathbf{k}$ grid where necessary to converge the spectrum. This greatly reduces the computational time and storage required when dealing with band structures that vary rapidly in some regions of the Brillouin zone and slowly in other regions and shall prove useful in other calculations involving Brillouin zone integrations.

V. CONCLUSIONS

We have presented a study of optical spin-injection rates in semiconductors GaAs, Si and CdSe using *ab initio* pseudopotential band structures. These allow (i) us to go beyond models applicable for only the band edge to investigate the spin-injection at higher energies and (ii) the potential to study more complicated materials for which a simple

ACKNOWLEDGMENTS

APPENDIX A: DETAILS OF THE MULTIPLE SCALE APPROACH

In this appendix, we outline a multiple scales approach to the density matrix dynamics response to pulsed excitation [Eq. (8)]. The multiple scales approach allows a separation of the different time scales: the pulse time, the carrier cycle, and the dephasing and loss times.

The electric field is written as

$$\mathbf{E}(t) = \mathbf{E}_{\mathrm{env}}(t)e^{-i\omega t} + \mathbf{E}_{\mathrm{env}}^{*}(t)e^{i\omega t},$$

where $\mathbf{E}_{\mathrm{env}}(t)$ is a slowly varying amplitude.

For the multiple scales treatment, we now put

$$\tau = \omega t$$

and introduce new functions for $\mathbf{E}(t)$, $\rho_{mn}(t)$, and so on that are given in terms of τ, and we then relabel these new functions as the old functions. We find

$$\frac{d\rho_{mn}(\tau)}{d\tau} = -i\frac{\hat{\omega}_{mn}}{\omega}(\mathbf{k})\rho_{mn}(\tau) - \frac{i}{\hbar\omega}([H^{\mathrm{ext}}(\tau),\rho(\tau)])_{mn} \tag{A1}$$

from Eq. (8), with $H^{\mathrm{ext}}(\tau) = -er^{a}E^{a}(\tau)$, and

$$\mathbf{E}(\tau) = \mathbf{E}_{\mathrm{env}}(\tau)e^{-i\tau} + \mathbf{E}_{\mathrm{env}}^{*}(\tau)e^{i\tau},$$

which we take as our basic equations. For the processes we consider, the intraband components[12] of r_{mn}^{a} make no contribution to the results, so for simplicity, we neglect them from the start. For convenience, we leave the **k** dependence of $\rho_{mn}(\tau)$ implicit [cf. Eq. (8)].

We now introduce

$$\tau_0 = \tau,$$

$$\tau_1 = \eta\tau,$$

where $\eta \ll 1$, and introduce different time scales into the problem by allowing our functions to formally depend on the variables τ_0 and τ_1, varying significantly only as each ranges over unity. Our "slowly varying envelope function" is thus so defined by writing

$$\mathbf{E}(\tau) = \mathbf{E}_{\mathrm{env}}(\tau_1)e^{-i\tau_0} + \mathbf{E}_{\mathrm{env}}^{*}(\tau_1)e^{i\tau_0}.$$

Now, we seek a solution of the form

$$\rho_{mn}(\tau) = \sum_{u=-\infty}^{\infty} e^{-iu\tau_0}\rho_{mn;u}(\tau), \tag{A2}$$

where the u are integers. We assume that the $\rho_{mn;u}(\tau)$ have no τ_0 dependence, and we specify the precise form we assume for them below.

Inserting Eq. (A2) into Eq. (A1), dimensionless terms such as $er_{mp}^{a}E^{a}(\tau_1)/\hbar\omega$ appear. We assume that they are of order η and write

$$\frac{er_{mp}^{a}E^{a}(\tau_1)}{\hbar\omega} = \eta\sigma_{mp}(\tau_1),$$

$$\frac{er_{mp}^{a}E^{a*}(\tau_1)}{\hbar\omega} = \eta\bar{\sigma}_{mp}(\tau_1),$$

etc., where the σ terms are of order unity or less. We then find

$$\frac{d\rho_{mn;u}(\tau)}{d\tau} = -i\left(\frac{\hat{\omega}_{mn}}{\omega} - u\right)\rho_{mn;u}(\tau) + i\eta[\sigma_{mp}(\tau_1)\rho_{pn;(u-1)}(\tau)$$
$$+ \bar{\sigma}_{mp}(\tau_1)\rho_{pn;(u+1)}(\tau) - \rho_{mp;(u-1)}(\tau)\sigma_{pn}(\tau_1)$$
$$- \rho_{mp;(u+1)}(\tau)\bar{\sigma}_{pn}(\tau_1)]. \tag{A3}$$

We now look for solutions of the form

$$\rho_{mn;u}(\tau) = \rho_{mn;u}^{(0)}(\tau_1) + \eta\rho_{mn;u}^{(1)}(\tau_1) + \eta^2\rho_{mn;u}^{(2)}(\tau_1) + \cdots,$$

where the $\rho_{mn;u}(\tau_1)$ are all assumed of the same order.

Putting

$$C_{mn;u} \equiv \left(\frac{\hat{\omega}_{mn}}{\omega} - u\right), \tag{A4}$$

we assume we have

$$C_{mn;u} = C_{mn;u}^{(0)} + \eta C_{mn;u}^{(1)},$$

and that for a given (mnu) either $C_{mn;u}^{(0)}$ survives or not; if it does survive, we include any purported $C_{mn;u}^{(1)}$ within it. So, for a given (mnu), not both of $C_{mn;u}^{(0)}$ and $C_{mn;u}^{(1)}$ will survive. However, because of the damping, we assume that both will not be nonzero, and thus precisely one of $C_{mn;u}^{(0)}$ and $C_{mn;u}^{(1)}$ will survive for a given (mnu).

Writing

$$\frac{\partial}{\partial\tau} = \frac{\partial}{\partial\tau_0} + \eta\frac{\partial}{\partial\tau_1} + \cdots,$$

we can now construct from Eq. (A3) a set of equations, one for each power of η. All our time dependence is now at the τ_1 level, so we write it simply as τ. We also leave off the explicit indication of time dependence. We can write the η^0 equation as

$$0 = C_{mn;u}^{(0)}\rho_{mn;u}^{(0)}, \tag{A5}$$

and the η^{i+1} equation as

$$\frac{\partial\rho_{mn;u}^{(i)}}{\partial\tau} = -iC_{mn;u}^{(0)}\rho_{mn;u}^{(i+1)} - iC_{mn;u}^{(1)}\rho_{mn;u}^{(i)} + iD_{mn;u}^{(i)}, \tag{A6}$$

with

$$D_{mn;u}^{(i)} = \sum_{p}(\sigma_{mp}\rho_{pn;(u-1)}^{(i)} + \bar{\sigma}_{mp}\rho_{pn;(u+1)}^{(i)})$$
$$- \sum_{p}(\rho_{mp;(u-1)}^{(i)}\sigma_{pn} + \rho_{mp;(u+1)}^{(i)}\bar{\sigma}_{pn}), \tag{A7}$$

where all quantities except the $C_{mn;u}^{(0)}$ and $C_{mn;u}^{(1)}$ depend on τ and the sum in Eq. (A7) is over the intermediate levels p.

We now separate the terms for which $C_{mn;u}^{(0)} = 0$ ("allowed" terms) from those for which $C_{mn;u}^{(0)} \neq 0$ ("forbidden" terms). We put

$$\rho^{(i)}_{mn;u} = \begin{cases} \alpha^{(i)}_{mn;u} & \text{if } C^{(0)}_{mn;u} = 0 \\ \beta^{(i)}_{mn;u} & \text{if } C^{(0)}_{mn;u} \neq 0. \end{cases} \tag{A8}$$

Then, from Eq. (A5), we find

$$\beta^{(0)}_{mn;u} = 0.$$

That is, the only components $\rho^{(0)}_{mn;u}$ that survive are the allowed terms.

From the $i=0$ level of Eq. (A6), we then find

$$\frac{\partial \alpha^{(0)}_{mn;u}}{\partial \tau} = -iC^{(1)}_{mn;u}\alpha^{(0)}_{mn;u} + ia_{mnu}A^{(0)}_{mn;u}, \tag{A9}$$

$$\beta^{(1)}_{mn;u} = \frac{b_{mnu}A^{(0)}_{mn;u}}{C^{(0)}_{mn;u}}, \tag{A10}$$

where

$$A^{(i)}_{mn;u} = \sum_p (\sigma_{mp}\alpha^{(i)}_{pn;(u-1)} + \bar{\sigma}_{mp}\alpha^{(i)}_{pn;(u+1)}) - \sum_p (\alpha^{(i)}_{mp;(u-1)}\sigma_{pn}$$
$$+ \alpha^{(i)}_{mp;(u+1)}\bar{\sigma}_{pn})$$

and

$$a_{mnu} = 1 \quad \text{and} \quad b_{mnu} = 0 \quad \text{if } C^{(0)}_{mn;u} = 0,$$

$$a_{mnu} = 0 \quad \text{and} \quad b_{mnu} = 1 \quad \text{if } C^{(0)}_{mn;u} \neq 0.$$

That is, the $\alpha^{(0)}_{mn;u}$ must be dynamically solved together, while the $\beta^{(1)}_{mn;u}$ are "slaved" to these solutions. At the $i=0$ level of Eq. (A6), we have solved, in principle, for the $\alpha^{(0)}_{mn;u}$ and $\beta^{(1)}_{mn;u}$. For $i>0$, we find that at the ith level of Eq. (A6), the known $\alpha^{(i-1)}_{mn;u}$ and $\beta^{(i)}_{mn;u}$ can be used to solve for the $\alpha^{(i)}_{mn;u}$ and $\beta^{(i+1)}_{mn;u}$. We do not explicitly give the straightforward but tedious calculation that confirms this.

We now look at our problem of interest, where we have two sets of levels. One set, corresponding to the conduction bands, we label by indices c, c', etc. The other set, corresponding to valence bands, we label by v, v', etc. Recalling Eqs. (A9) and (A10), we take $C^{(0)}_{cc';0} = 0$ and $C^{(0)}_{vv';0} = 0$, since the conduction bands are supposed to be close to each other, and the valence bands close to each other. Further, since we consider one-photon processes, we take $C^{(0)}_{cv;1} = 0$ and $C^{(0)}_{vc;-1} = 0$. All other $C^{(0)}_{mn;u}$ we take to be nonzero. Thus the only nonzero $\alpha^{(0)}_{mn;u}$ are $\alpha^{(0)}_{cv;1}$, $\alpha^{(0)}_{vc;-1}$, $\alpha^{(0)}_{cc';0}$, and $\alpha^{(0)}_{vv';0}$. Collecting the terms that appear in the Eq. (A9) and dropping the superscript (0), we have

$$i\frac{\partial \alpha_{cv;1}}{\partial \tau} = C^{(1)}_{cv;1}\alpha_{cv;1} - \sum_{v'} \sigma_{cv'}\alpha_{v'v;0} + \sum_{c'} \alpha_{cc';0}\sigma_{c'v},$$

$$i\frac{\partial \alpha_{vc;-1}}{\partial \tau} = C^{(1)}_{vc;-1}\alpha_{vc;-1} - \sum_{v'} (\bar{\sigma}_{vc}\alpha_{cc';0} - \alpha_{vv';0}\bar{\sigma}_{v'c}),$$

$$i\frac{\partial \alpha_{cc';0}}{\partial \tau} = C^{(1)}_{cc';0}\alpha_{cc';0} - \sum_v (\sigma_{cv}\alpha_{vc';-1} - \alpha_{cv;1}\bar{\sigma}_{vc'}),$$

$$i\frac{\partial \alpha_{vv';0}}{\partial \tau} = C^{(1)}_{vv';0}\alpha_{vv';0} - \sum_c (\bar{\sigma}_{vc}\alpha_{cv';1} - \alpha_{vc;-1}\sigma_{cv'}). \tag{A11}$$

These equations are capable of deriving full excitation and saturation of the upper levels. No perturbation theory approximations have yet been made about where the population initially lies and by how much the initial population is depleted. If the field is long enough, full cycling can, in principle, occur. The only approximations have to do with the slowness of the variation in the envelope function, the weakness of the external perturbation, and the weakness of the dephasing and damping.

We can now go to a perturbative result by putting $\alpha_{vv';0} \approx \delta_{vv'}$ throughout the time of integration and solving approximately for the other terms. Assuming that the field is turned on after $\tau=0$, we can solve for $\alpha_{cv;1}(\tau)$ and $\alpha_{vc;-1}(\tau)$. We insert these into the third equation of Eq. (A11), and we evaluate the resulting integrals in the limit that the envelope function is essentially constant once it is turned on. Then, for times τ much longer than damping and dephasing times we have, for example,

$$\int_0^\tau d\tau' e^{-iC^{(1)}_{vc;-1}\tau'}\bar{\sigma}_{vc} = \frac{e^{-iC^{(1)}_{vc;-1}\tau} - 1}{(-iC^{(1)}_{vc;-1})}\bar{\sigma}_{vc}, = \frac{\bar{\sigma}_{vc}}{iC^{(1)}_{vc;-1}},$$

for $\bar{\sigma}_{vc}$ essentially constant and τ long enough. Similarly,

$$\int_0^\tau d\tau' e^{-iC^{(1)}_{cv;1}\tau'}\sigma_{cv} \approx \frac{\sigma_{cv}}{iC^{(1)}_{cv;1}}.$$

This then yields

$$\frac{\partial \alpha_{cc';0}}{\partial \tau} = -iC^{(1)}_{cc';0}\alpha_{cc';0} + \frac{1}{i}\sum_v \left(\frac{\sigma_{cv}\bar{\sigma}_{vc'}}{C^{(1)}_{vc';-1}} + \frac{\sigma_{cv}\bar{\sigma}_{vc'}}{C^{(1)}_{cv;1}} \right).$$

Dropping the η's and reintroducing the time t, we have

$$\frac{\partial \alpha_{cc';0}}{\partial t} = -i(\omega_{cc'} - i\Gamma_{cc'})\alpha_{cc';0} + \frac{e^2 E^a E^{b*}}{i\hbar^2}$$
$$\times \sum_v \left(\frac{r^a_{cv}r^b_{vc'}}{\omega - \omega_{c'v} - i\Gamma_{vc'}} - \frac{r^a_{cv}r^b_{vc'}}{\omega - \omega_{cv} + i\Gamma_{cv}} \right)$$

If we take the $\Gamma_{vc'}$ and Γ_{cv} to be small, we recover Eq. (11).

APPENDIX B: DETAILS ON THE NUMERICAL BRILLOUIN ZONE INTEGRATION

Integrations over the BZ are typically simplified by using only k points in an irreducible "wedge" of the BZ. At any k point outside a specified irreducible wedge, the matrix elements $\mathbf{r}_{mn}(\mathbf{k})$ can be determined from the matrix elements at an equivalent point inside the irreducible wedge via the point group operation relating the two k points. We denote the number of point group operations in the BZ by N_{sym}. This will include the inversion operator even if the crystal is not centrosymmetric, as long as the Hamiltonian exhibits time reversal symmetry. The BZ can be divided into N_{sym} symme-

try related, nonoverlapping irreducible wedges of equal volume. Starting with the set of k points, making one wedge and applying each point group operation produce N_{sym} symmetry related wedges.

For each point group symmetry operation, characterized by a 3×3 matrix α, the velocity matrix elements [see Eq. (6)] satisfy the relation

$$v_{mn}^a(\boldsymbol{\alpha}\mathbf{k}) = \alpha^{ab} v_{mn}^b(\mathbf{k}), \tag{B1}$$

the spin matrix elements satisfy

$$S_{mn}^a(\boldsymbol{\alpha}\mathbf{k}) = \det(\boldsymbol{\alpha}) \alpha^{ab} S_{mn}^b(\mathbf{k}), \tag{B2}$$

and the energy eigenvalues satisfy

$$\omega_m(\boldsymbol{\alpha}\mathbf{k}) = \omega_m(\mathbf{k}). \tag{B3}$$

The determinant $\det(\boldsymbol{\alpha})$ is $+1$ for proper rotations and -1 for improper ones.

Since there is still an inversion symmetry in the BZ even if the crystal has no center of inversion, this symmetry can be used to further reduce the k points. In particular, the states can always be chosen so that

$$\omega_m(-\mathbf{k}) = \omega_m(\mathbf{k}), \tag{B4}$$

$$v_{mn}^a(-\mathbf{k}) = -v_{nm}^a(\mathbf{k}), \tag{B5}$$

and

$$S_{mn}^a(-\mathbf{k}) = S_{nm}^a(\mathbf{k}). \tag{B6}$$

For the noncentrosymmetric crystals, N_{sym} is then effectively twice the number of point group operations.

When calculating a scalar quantity, such as the electron density or total energy, the contribution to the integral from each irreducible wedge is equivalent. In those cases, the integral over the full BZ can be found simply by integrating over an irreducible wedge and multiplying the result by N_{sym}. In the case of scalars, from the general form Eq. (18), we have

$$G_{cv}(\omega) = N_{\text{sym}} G_{w|cv}(\omega) = N_{\text{sym}} \int_w \frac{d^3k}{8\pi^3} g_{cv}(\mathbf{k}) \delta[\omega - \omega_{cv}(\mathbf{k})], \tag{B7}$$

where the subscript w on the integral symbol indicates that the integral should be done over an irreducible wedge. For the tensor quantities in which we are interested, this protocol would be incorrect, since the contribution from one irreducible wedge is generally different than that from another wedge. One way to proceed, which we adopt in this work, is to use an equivalent scalar representation of the desired tensor component. The integrand for this expression transforms throughout reciprocal space as a scalar, and so the integral over any irreducible wedge gives the same result. Each tensor component is invariant under the point group symmetry operations, and so for a specific component $\xi^{ij}(\omega)$, the equivalent scalar representation is

$$\xi^{ij}(\omega) = \frac{1}{N_{\text{sym}}} \sum_{s=1}^{N_{\text{sym}}} \alpha_s^{ia} \alpha_s^{jb} \xi^{ab}(\omega), \tag{B8}$$

where s indexes the symmetry operations. From Eq. (16), this gives

$$\xi^{ij}(\omega) = \frac{2e^2\pi}{\hbar^2 N_{\text{sym}}} \int_w \frac{d^3k}{8\pi^3} \sum_{c,v} \sum_{s=1}^{N_{\text{sym}}} \alpha_s^{ia} \alpha_s^{jb} r_{cv}^a(\mathbf{k}) r_{vc}^b(\mathbf{k}) \delta[\omega$$
$$- \omega_{cv}(\mathbf{k})], \tag{B9}$$

which more accurately reflects how we compute $\xi^{ab}(\omega)$. The spin-injection rate is described by a third rank pseudotensor, and so for a particular component $\zeta^{hij}(\omega)$, we have

$$\zeta^{hij}(\omega) = \frac{1}{N_{\text{sym}}} \sum_{s=1}^{N_{\text{sym}}} \det(\boldsymbol{\alpha}_s) \alpha_s^{ha} \alpha_s^{ib} \alpha_s^{jc} \zeta^{abc}(\omega). \tag{B10}$$

From Eq. (13) this gives

$$\zeta^{hij}(\omega) = \frac{\pi e^2}{\hbar^2 N_{\text{sym}}} \int_w \frac{d^3k}{8\pi^3}$$
$$\times \sum_{c,c',v}{}' \sum_{s=1}^{N_{\text{sym}}} \det(\alpha_s) \alpha_s^{ha} \alpha_s^{ib} \alpha_s^{jc} S_{c'c}^a r_{vc'}^a r_{cv}^b (\delta[\omega_{cv}(\mathbf{k})$$
$$- \omega] + \delta[\omega_{c'v}(\mathbf{k}) - \omega]). \tag{B11}$$

Evaluating the s sum over the symmetries determines which tensor and pseudotensor components are nonzero. For the zinc-blende and diamond crystals, the only nonzero components of ξ^{ab} are $\xi^{xx} = \xi^{yy} = \xi^{zz}$. For the spin-injection tensor, the only nonunique component is ζ^{xyz}. The other nonzero components are related to it by Eq. (22). Note that the rank-3 tensors for bulk silicon that describe typical second-order nonlinear optical effects are all zero because of inversion symmetry. However, the pseudotensor describing the spin-injection rate is nonzero for the same components, as in the zinc-blende crystals.

To obtain a tetrahedral grid throughout the BZ, we use the improved tetrahedron method introduced by BJA.[7] The procedure works for any crystal class and allows us to avoid any tedious by-hand chopping procedure. However, even with this scheme, tens of thousands inequivalent k points can be required if the function being integrated is complicated enough, as can arise even for the simplest semiconductors. Although this is not really a difficulty for the **k·p** method, since calculating the states for each k point at most requires diagonalizing a 30×30 matrix, it can be problematic in an *ab initio* code where the calculation time per k point can be substantial.

Following BJA, we divide the three reciprocal lattice vectors into n_1, n_2, and n_3 divisions, producing $n_1 \times n_2 \times n_3$ parallelepipeds. The number of divisions along each axis should be chosen to respect the crystal symmetry, so that the mesh transforms onto itself under the symmetry operations. We then find the set of irreducible k points and tetrahedra as described by BJA: Each k point is represented by the integer vector (i,j,m) along the divided reciprocal lattice vectors, where i runs from 0 to $M-1$, j runs from 0 to $N-1$, and m

runs from 0 to $P-1$. We create a pointer array where each k point is identified by the an integer index $(i+j) \times (M+m) \times N \times M$ running from 0 to $M \times N \times P$. We cycle over the k points, beginning at the k point with index 1. We apply each symmetry matrix α_s to the k point, and if the transformed k point has a lower index, then the pointer index for the current k point is replaced by the lower index of the transformed point. This is done for each k point in sequence, until we have exhausted the list, and our pointer-list points every k point to an equivalent irreducible k point.

Each parallelepiped is then divided into six equal volume tetrahedra as specified by BJA. The first division is along the shortest diagonal into two triangular prisms, and then each prism is divided into three tetrahedra (see Fig. 1 in BJA[7] for a schematic on how to divide the parallelepiped). Each tetrahedron is identified by the four integer indices of the corner k points. The corners of one tetrahedron can be symmetry related to the corners of many others. All these equivalent tetrahedra can be replaced by a single tetrahedron and a multiplicity factor. If the k points have been reduced as specified above, then the symmetry-equivalent tetrahedra will have the same set of four indices, and so the equivalent tetrahedra can be easily identified by sorting the tetrahedra with respect to their indices.

The contributions from each tetrahedron are summed to give the total spectrum. The LATM formula we use linearly interpolates the energies in the δ function and linearly interpolates the integrand using the values at the tetrahedron corners. The spectrum is then calculated again with a finer grid throughout the BZ. This spectrum is compared to the previous spectrum, and the frequency ranges where the spectrum has not converged are identified. To improve the spectrum, one can simply, and inefficiently, increase the density of the grid uniformly throughout the BZ. However, this refines the grid even in volumes where refining is unnecessary. To focus on the BZ regions that need refining, we first loop over the submesh units (parallelepipeds) that make up the full BZ and identify the ones that need to be refined. For each submesh unit, we find the frequency range specified by the minimum to maximum values of $\omega_{cv}(\mathbf{k})$. If the spectrum is to be refined at a frequency within this range, then the submesh unit is labeled as one to be refined. Once we have labeled all the desired submesh units, they are divided into eight smaller submesh units. At the next level of refinement, we double the indices n_1, n_2, and n_3, without creating a new uniform grid, and relabel all the k points from the previous iteration with respect to the new doubled indices. When we divide a submesh unit, we divide it into eight similar units and introduce 19 new k points to our list of k points: one at the center of each face, one at the midpoint of each edge, and one at the center of the submesh unit as sketched out in Fig. 12. Each of the eight smaller submesh units is then divided into six equal volume tetrahedra using the same idea as BJA.

Instead of dividing the submesh units as we do, one could directly divide the more primitive tetrahedral microzones. However, part of the ease and efficiency of the BJA scheme in finding the irreducible k points is based on the integer representation of the k points, and we wish to maintain this integer representation in our subdivisions. Of the multitude of ways to divide a tetrahedron into smaller tetrahedra, the
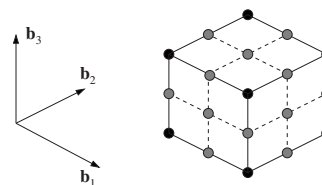

FIG. 12. Dividing a submesh unit into eight smaller similar, units. The black points represent points from the previous iteration, and the solid lines represent the submesh edges from the previous iteration. The gray points are the new points in the adaptive routine, and the dashed lines represent the edges of the new submesh units. Including the points that are on the back faces of the parallelepiped, there are 19 new points.

simplest possible way to keep an integer representation of the k points would be to divide the tetrahedron edges at their midpoints. This would produce eight smaller tetrahedra, but not of all equal volume. By using our slightly more complicated scheme, we produce equal volume tetrahedra at each iteration of refinement, and it is easy to keep track of the tetrahedra volumes without keeping track of each individual tetrahedron. We find that the region of the BZ that needs to be divided is usually larger than a single tetrahedron anyway, so we would not gain much by adding the option to divide the tetrahedra individually.

When a submesh unit is found that is to be divided, the 19 new k points are temporarily stored. These are appended to the current list of k points. However, before this is done, we check that each new k point does not already exist in the list of k points. If an adjacent submesh unit was previously refined, then the newly introduced k points on the shared face will already exist, so we do not need to include these points again. Once we have the new complete list of k points, which consists of the list of reduced k points from the previous iteration and the unreduced k points just found, we then identify the irreducible points by again using the algorithm of BJA. One might expect that the set of newly determined k points can be reduced within itself, so that none of the newly found k points are symmetry related to a k point from an older set. Although this is generally true, there are a few special cases where a new k point along the edge of a submesh unit can be reduced to an irreducible k point from the original grid. One can neglect this detail and just treat the k points as unique, but we have decided to fully reduce the set of k points after the refinement. The new submesh units are then divided into tetrahedra, and the symmetry related tetrahedra of this subset are found and reduced, as was done for the initial grid. With the tetrahedra determined, we then calculate the matrix elements at the new points and calculate the spectrum as before for this nonuniform grid. The resulting spectrum can be compared to the one from the previous iteration, and if further refinement is required, the same process can be repeated until the desired accuracy is achieved.

To illustrate the method and emphasize the efficiency gained with this adaptive scheme, we use the pseudopotential calculation of $\xi^{xx}(\omega)$ for GaAs as an example. We use the theoretical lattice constant, since it reproduces well the band-edge features, as detailed in Sec. IV of the main text. In Fig.
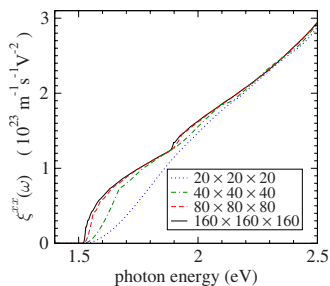
FIG. 13. (Color online) The resulting $\xi^{xx}(\omega)$ spectrum from different refinement levels of our adaptive grid scheme. We see that convergence is reached with a grid that would be equivalent to an $80 \times 80 \times 80$ grid throughout the full BZ.

13, we show the spectrum at different levels of grid refinement up to 1 eV above the absorption edge. The dash-dotted spectrum was produced using a uniform tetrahedral grid produced from dividing each reciprocal lattice vector into 20 divisions. After this grid is symmetry reduced as instructed by BJA, the number of inequivalent k points is reduced to only 256. A grid this coarse is clearly not useful for exploring properties near the band edge: the expected square-root turn on is missing, as is any indication of a split-off energy at 0.35 eV above the band edge, where the split-off band is excited. Other examples of the difficulty in converging the spectrum in this region for GaAs exist. For example, see the low-energy part of the $\epsilon_2(\omega)$ spectrum in Fig. 2 of Monachesi *et al.*[60] To produce a better spectrum, we search through the BZ and find which submesh units contribute to the spectrum below 3 eV. New k points are introduced to divide these submesh units into smaller units as discussed above. This gives us a grid which, in the relevant region, is the same as a grid obtained by dividing the axes into 40 divisions. Symmetry reducing this grid reduces it to 373 k points, or only 117 new k points to be evaluated. The resulting spectrum is shown in Fig. 13 by the thin dashed line. The change from the original spectrum suggests that the calculation is not yet converged, so we refine the grid again. This
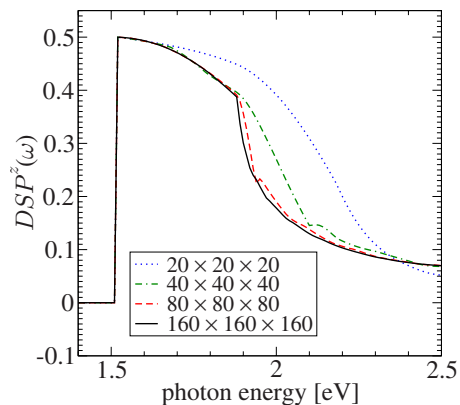

FIG. 14. (Color online) The resulting $DSP^z(\omega)$ spectrum from different refinement levels of our adaptive grid scheme. We see that convergence is reached with a grid that would be equivalent to an $80 \times 80 \times 80$ grid throughout the full BZ.

gives 584 new k points, and the resulting spectrum given by the thick dashed lines begins to show the features we expect. Finally, to satisfy ourselves that this is converged, we refine the grid once more. This requires 3112 new k points but is effectively the same as starting with a 160 $\times 160 \times 160$ divisions, or 4×10^6 k points. It should be noted that the uniform grid throughout the full BZ would end up requiring 90 241 k points in the irreducible zone, or 22 times more k point evaluations than our adaptive scheme to arrive at the same accuracy in the spectrum. Our final converged spectrum is given by the unbroken line in Fig. 13.

In Fig. 14 we show the convergence of the degree of spin polarization with increasing grid resolution. It is clear that the sharp turn in the spectrum at roughly 1.9 eV, corresponding to the split-off energy, is smeared out for lower resolutions. However, the degree of spin polarization near the band edge (50%) is reproduced with our coarsest grid.

[1] *Optical Orientation, Modern Problems in Condensed Matter Physics*, edited by F. Meier and B. P. Zakharchenya (North-Holland, Amsterdam, 1984).

[2] I. Zutic, J. Fabian, and S. D. Sarma, Rev. Mod. Phys. **76**, 323 (2004).

[3] R. D. R. Bhat and J. E. Sipe, arXiv:cond-mat/0601277 (unpublished).

[4] G. Y. Guo, Y. Yao, and Q. Niu, Phys. Rev. Lett. **94**, 226601 (2005).

[5] Y. Yao and Z. Fang, Phys. Rev. Lett. **95**, 156601 (2005).

[6] R. D. R. Bhat, F. Nastos, A. Najmaie, and J. E. Sipe, Phys. Rev. Lett. **94**, 096603 (2005).

[7] P. E. Blöchl, O. Jepsen, and O. K. Andersen, Phys. Rev. B **49**, 16223 (1994).

[8] S. Richard, F. Aniel, and G. Fishman, Phys. Rev. B **70**, 235204 (2004).

[9] S. Richard, F. Aniel, and G. Fishman, Phys. Rev. B **71**, 169901(E) (2005).

[10] G. Lampel, Phys. Rev. Lett. **20**, 491 (1968).

[11] E. N. Adams, J. Chem. Phys. **21**, 2013 (1953).

[12] E. I. Blount, Solid State Phys. **13**, 305 (1962).

[13] A. Najmaie, R. D. R. Bhat, and J. E. Sipe, Phys. Rev. B **68**, 165348 (2003).

[14] D. J. Hilton and C. L. Tang, Phys. Rev. Lett. **89**, 146601 (2002).

[15] G. Dresselhaus, Phys. Rev. **100**, 580 (1955).

[16] A. N. Chantis, M. van Schilfgaarde, and T. Kotani, Phys. Rev. Lett. **96**, 086405 (2006).

[17] Although the expressions in this paper are all in Gaussian units, the figure plots of the spectra are presented in SI mks. When converting units, one must be careful since the basic electromag-

netic quantities are defined differently in the different systems. For purposes of presentation, we have chosen to keep the phenomenological formulas Eq. (3) and (15) the same in both systems and have modified the microscopic formula for ξ^{ab} and ζ^{abc} to accommodate the SI-mks system. In the SI-mks system, $\text{Im}[\epsilon^{ab}(\omega)]/\epsilon_\circ = \text{Im}[\chi^{ab}(\omega)] = 2\pi\hbar\xi^{ab}(\omega)$; in the Gaussian system, $\text{Im}[\epsilon^{ab}(\omega)] = 4\pi\,\text{Im}[\chi^{ab}(\omega)] = 2\pi\hbar\xi^{ab}(\omega)$.

[18] First-principles computation of material properties: the ABINIT software project. X. Gonze, J.-M. Beuken, R. Caracas, F. Detraux, M. Fuchs, G.-M. Rignanese, L. Sindic, M. Verstraete, G. Zerah, F. Jollet, M. Torrent, A. Roy, M. Mikami, Ph. Ghosez, J.-Y. Raty, and D. C. Allan, Comput. Mater. Sci. **25**, 478 (2002); www.abinit.org

[19] C. Hartwigsen, S. Goedecker, and J. Hutter, Phys. Rev. B **58**, 3641 (1998).

[20] S. Goedecker, M. Teter, and J. Hutter, Phys. Rev. B **54**, 1703 (1996).

[21] B. S. Mendoza, F. Nastos, N. Arzate, and J. E. Sipe, Phys. Rev. B **74**, 075318 (2006).

[22] A. J. Read and R. J. Needs, Phys. Rev. B **44**, 13071 (1991).

[23] H. Kageshima and K. Shiraishi, Phys. Rev. B **56**, 14985 (1997).

[24] R. O. Jones and O. Gunnarsson, Rev. Mod. Phys. **61**, 689 (1989).

[25] R. W. Godby, M. Schlüter, and L. J. Sham, Phys. Rev. Lett. **56**, 2415 (1986).

[26] Z. H. Levine and D. C. Allan, Phys. Rev. Lett. **63**, 1719 (1989).

[27] Z. H. Levine and D. C. Allan, Phys. Rev. Lett. **66**, 41 (1991).

[28] R. Del Sole and R. Girlanda, Phys. Rev. B **48**, 11789 (1993).

[29] F. Nastos, B. Olejnik, K. Schwarz, and J. E. Sipe, Phys. Rev. B **72**, 045223 (2005).

[30] M. Cardona and F. H. Pollak, Phys. Rev. **142**, 530 (1966).

[31] E. X. Wang, M. D. Giles, S. Yu, F. A. Leon, A. Hiroki, and S. Odanaka, *Simulation of Semiconductor Processes and Devices (SISPAD)*, Proceedings of SISPAD (IEEE Electron Devices Society, Tokyo, 1996), No. 1, p. 67.

[32] J. Henk, Phys. Rev. B **64**, 035412 (2001).

[33] S. Q. Wang and H. Q. Ye, Phys. Rev. B **66**, 235111 (2002).

[34] N. Fraj, S. Ben Radhia, and K. Boujdaria, Solid State Commun. **142**, 342 (2007).

[35] C. Weisbuch and C. Hermann, Phys. Rev. B **15**, 816 (1977).

[36] J. L. P. Hughes, Y. Wang, and J. E. Sipe, Phys. Rev. B **55**, 13630 (1997).

[37] R. Asahi, W. Mannstadt, and A. J. Freeman, Phys. Rev. B **59**, 7486 (1999).

[38] B. Adolph and F. Bechstedt, Phys. Rev. B **57**, 6519 (1998).

[39] A. Dal Corso, F. Mauri, and A. Rubio, Phys. Rev. B **53**, 15638 (1996).

[40] O. Pulci, G. Onida, A. I. Shkrebtii, R. Del Sole, and B. Adolph, Phys. Rev. B **55**, 6685 (1997).

[41] M. Oestreich, M. Bender, J. Hübner, D. Hägele, W. W. Rühle, T. Hartmann, P. J. Klar, W. Heimbrodt, M. Lampalzer, K. Volz, and W. Stolz, Semicond. Sci. Technol. **17**, 285 (2002).

[42] J. M. Kikkawa, J. A. Gupta, I. Malajovich, and D. D. Awschalom, Physica E (Amsterdam) **9**, 194 (2001).

[43] D. D. Awschalom and J. M. Kikkawa, Phys. Today **52** (6), 33 (1999).

[44] M. J. Stevens, R. D. R. Bhat, J. E. Sipe, H. M. van Driel, and A. L. Smirl, Phys. Status Solidi B **238**, 568 (2003).

[45] D. T. Pierce and F. Meier, Phys. Rev. B **13**, 5484 (1976).

[46] H.-J. Drouhin, C. Hermann, and G. Lampel, Phys. Rev. B **31**, 3872 (1985).

[47] N. Bagraev, L. Vlasenko, and R. Zhitnikov, Sov. Phys. JETP **44**, 500 (1976).

[48] A. S. Verhulst, Ph.D. thesis, Stanford University, 2004.

[49] A. S. Verhulst, I. G. Rau, Y. Yamamoto, and K. M. Itoh, Phys. Rev. B **71**, 235206 (2005).

[50] F. Roux, G. Lampel, Y. Lassailly, and J. Peretti, Bull. Am. Phys. Soc. **20** (12), V20.00012 (2006).

[51] G. Lampel, in Ninth International Conference on the Physics of Semiconductors, 1968 (unpublished), p. 1139.

[52] G. Grosso and G. P. Parravacini, *Solid State Physics* (Academic, New York, 2000).

[53] L. C. Lew Yan Voon, M. Willatzen, M. Cardona, and N. E. Christensen, Phys. Rev. B **53**, 10703 (1996).

[54] S. L. Chuang and C. S. Chang, Phys. Rev. B **54**, 2491 (1996).

[55] D. J. Dugdale, S. Brand, and R. A. Abram, Phys. Rev. B **61**, 12933 (2000).

[56] J. A. Gupta, D. D. Awschalom, A. L. Efros, and A. V. Rodina, Phys. Rev. B **66**, 125307 (2002).

[57] A. Bonnot, R. Planel, and C. B. à la Guillaume, Phys. Rev. B **9**, 690 (1974).

[58] M. A. Chamarro, C. Gourdon, and P. Lavallard, Semicond. Sci. Technol. **8**, 1868 (1993).

[59] Y. G. Kusrayev, A. V. Koudinov, B. P. Zakharchenya, S. Lee, J. K. Furdyna, and M. Dobrowolska, Phys. Rev. B **72**, 155301 (2005).

[60] P. Monachesi, A. Marini, G. Onida, M. Palummo, and R. Del Sole, Phys. Status Solidi B **184**, 101 (2001).